

Theory of Optomechanical Locking in Driven-Dissipative Coupled Polariton Condensates

I. A. Ramos Pérez,^{1,2,*} I. Carraro Haddad,^{1,2,*} F. Fainstein,^{3,4,*} D. L. Chafatinos^{1,2},
G. Usaj^{1,2,5,6}, G. B. Mindlin,^{3,4} A. Fainstein^{1,2} and A. A. Reynoso^{1,2,7,†}

¹*Centro Atómico Bariloche and Instituto Balseiro, Comisión Nacional de Energía Atómica (CNEA)- Universidad Nacional de Cuyo (UNCUYO), 8400 Bariloche, Argentina.*

²*Instituto de Nanociencia y Nanotecnología (INN-Bariloche),*

Consejo Nacional de Investigaciones Científicas y Técnicas (CONICET), Argentina.

³*Departamento de Física, FCEyN, Universidad de Buenos Aires, Buenos Aires 1428, Argentina.*

⁴*IFIBA, CONICET, Buenos Aires 1428, Argentina.*

⁵*TQC, Universiteit Antwerpen, Universiteitsplein 1, B-2610 Antwerpen, Belgium*

⁶*CENOLI, Université Libre de Bruxelles - CP 231, Campus Plaine, B-1050 Brussels, Belgium*

⁷*Departamento de Física Aplicada II, Universidad de Sevilla, E-41012 Sevilla, Spain.*

(Dated: December 29, 2023)

Synchronization between distant polariton condensates has been theoretically proposed and experimentally observed. It is a quite general behaviour intimate to dynamical dissipative non-linear systems, and pervasive to very different domains of nature. We theoretically study these phenomena for two coupled condensates in the presence of a fixed mechanical harmonic driving representing an electrically generated modulation, through coherent bulk acoustic waves, or self-induced optomechanical vibrations. We consider either a linear or a quadratic phonon-displacement induced modulation of the coupling between the condensates. Peculiar asynchronously locked phases are found, and are analyzed in the context of synchronization and Josephson-like oscillations phenomena that appear in the non-driven case. Some analytical analysis of the asynchronous locking is performed in the rotating wave approximation, while the more general situation is studied numerically. Arnold tongues corresponding to the asynchronously locked phases develop at condensate detunings that correspond to integer numbers of the mechanical frequency and also to rational fractions of it. Unlocked 'quasiperiodic' and chaotic regimes can also be reached. In particular, the phonon-induced fractional locking frequencies arrange in a Farey sequence that produces a Devil's staircase of the steady-state dressed detuning between the condensates. Importantly, both polariton-polariton and reservoir-polariton interactions facilitate the realization of phonon-induced asynchronously locked phases. The relation to recent experiments on optomechanically driven condensates in arrays of polariton traps is discussed.

I. INTRODUCTION

Microcavity exciton-polariton fluids, a quantum state of matter formed by strongly coupled excitons and photons in microcavities made from semiconductors, constitute a hybrid system [1] that displays a plethora of interesting properties. These include, among others, Bose-Einstein condensation [2], superfluidity [3], and Josephson-like oscillations [4, 5]. While these fluids bear some similarities with more standard quantum phases in interacting equilibrium systems, there are several peculiar aspects that arise from their driven-dissipative non-equilibrium nature that makes them specially interesting, even more nowadays with well established ideas on the field of non-hermitian dynamics [6]. The recent blooming of polariton related research has been strongly supported on the degree of maturity that the experimental capability of engineering controllable coupled polariton traps has attained, either in pairs [4, 5] or forming arrays of different geometries and dimensionalities [7–11]. This has allowed, for instance, the implementation of quantum simulators [12–15] and the exploration of different topological properties of known lattice models [16], profiting from the experimental possibility of accessing excited states and/or controlling interactions among

polaritons.

In parallel, another emerging area is that of cavity optomechanics, hybrid structures that bridge the optical domain with acoustics [17–20]. Optomechanical resonators and optomechanical crystals exploit the co-localisation of mechanical and optical modes to greatly enhance their interaction. Non-linearities arising in this context due to dynamical feedback lead, e.g., to the optical cooling of the mechanical oscillator down to its quantum ground state [21–24], and also to mechanical self-oscillation conceptually similar to phonon lasing [25, 26]. The field of cavity optomechanics has recently been connected with that of exciton-polariton fluids in semiconductor microcavities by the serendipitous observation that the same GaAs/AlAs based distributed Bragg reflector planar microcavities leading to cavity polaritons also confine hypersound in the GHz range [27, 28]. This is particularly relevant in view of the potential access to a very strong optomechanical coupling mediated by excitons and based on the deformation potential interaction [29, 30]. In fact, it has been recently shown that GHz coherent mechanical waves that strongly modulate the polariton states can be either self-induced by continuous wave optical excitation [31–34], or externally injected using piezoelectric bulk acoustic wave (BAW) transducers [34–36]. These resources expand the cavity-optomechanics toolkit that, for example, could be used to implement effective gauge potentials in polaritonics based on the mechanically induced dynamic modulation of inter-site coupling in lattices, as originally proposed to demonstrate

* These three authors contributed equally

† Corresponding author, e-mail: reynoso@cab.cnea.gov.ar

the photonic Aharonov-Bohm effect in photonic fibers [37], and more recently non-Hermitian chiral phononics in photonic crystal nano-beams [38].

Our aim is to study the behaviour of driven-dissipative coupled light fluids intertwined with coherent vibrations to yield a new collective behaviour. We search for the Floquet engineering of the polaritons with these mechanical waves to dynamically control these systems. We theoretically address these questions and to that aim we analyze a model system consisting of two traps populated by non-equilibrium coupled polariton condensates. These coupled condensates are subject to an optomechanically induced vibrational driving involving GHz phonons of the traps. This is done with realistic experimental implementations in mind. The proposed problem naturally connects with that of synchronization and Josephson oscillations in non-Hermitian coupled polariton condensates [39–43], so we start our analysis discussing this problem from a dynamical system’s point of view. We then consider the effect of the mechanical perturbation first in a rotating wave approximation (RWA), and then through a full numerical modeling of the problem. We study two experimentally relevant cases in which the mechanics modulates either linearly or quadratically the inter-site coupling. We show that striking signatures of the coherent polariton-phonon coupling emerge when the structures are optically driven with a continuous non-resonant optical excitation above the threshold for condensation: states of the polariton condensates at neighbor traps asynchronously lock with energies differing by integer numbers of the confined phonon energy, and also by rational fractions of it. The conditions under which this new synchronized phase is stable are analyzed, and the resulting dynamics is investigated. Finally, concluding remarks and proposals for the experimental implementation of these findings are presented.

II. THE PHYSICAL SYSTEM

The physical system considered consists on pairs of coupled μm -sized traps based on distributed Bragg reflector (DBR) cavities as those previously studied in the context of polariton phenomena [6]. These polariton traps can be originated in planar microcavities due to intrinsic disorder [4, 42], can be fabricated by deep etching of microcavity pillar-like structures [5, 44], created by micro-structuring the spacer of a microcavity in-between growth steps performed by molecular beam epitaxy (MBE) [8, 9, 31], or using laser-induced effective potentials [43]. The same kind of semiconductor layered structures can be designed to perform as an acoustic phonon cavity with confined vibrational states [45]. Similar to polaritons, these confined phonon states can be engineered as molecular-like levels in double-structures or to form tailored engineered phonon bands in lattices [46]. Interestingly, the same sequence of layer thicknesses designed to optimize a photon cavity lead to an optimum phonon cavity, with perfect overlap of the photon and phonon fields allowing for the conception of high performance optomechanical resonators operating in the tens of GHz range [27, 47–50]. As we will see, this allows for the mechanically induced modulation of the

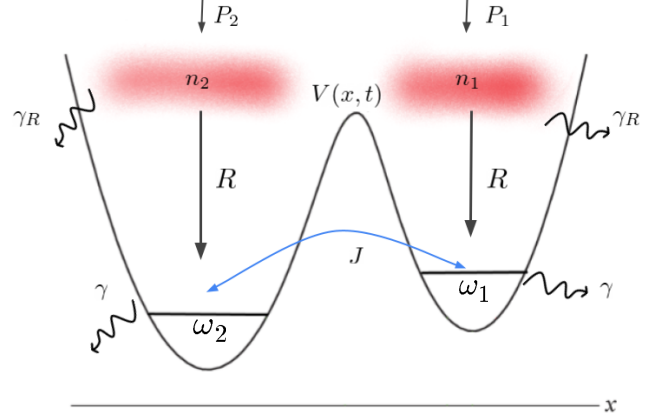


Figure 1. Scheme of polariton condensates in a pair of coupled traps. ω_j is the bare frequency the j -mode (for clarity in the scheme a single confined state is assumed per trap), J describes a direct hopping rate term between modes (determined by the potential $V(x, t)$), γ is the polariton decay rate and R the stimulated loading rate from the reservoir. The dynamic of the later is controlled by the pump power P_j , the excitonic decay rate γ_R and the stimulated decay to the condensate. The time dependence in the potential $V(x, t)$ arises from the modulation introduced by a coherent mechanical wave, and which can affect the hopping rate J . Polaritons are affected by Coulomb interactions through U_j^P and U_j^R , the polariton-polariton and reservoir-polariton couplings, respectively (not shown).

inter-site coupling in polaritonic lattices.

Two mechanisms contribute to the photon-phonon interaction in these DBR-based microcavity structures, namely, radiation pressure (related to the phonon induced displacement of the cavity interfaces) and electrostriction (related to the phonon induced shift of electronic levels induced by deformation potential interaction [51]). These two mechanisms are of similar magnitude far away from electronic resonances, but electrostriction can be enhanced by several orders of magnitude by excitonic resonances which are intrinsic to the exciton-photon strong coupling regime [29, 30, 49, 50].

Indeed, polaritons in the proposed resonators originate from the strong resonant coupling between the confined photon modes and excitons in quantum wells that are embedded in the cavity spacer [6]. Thus this system naturally becomes a playing ground to also exploit exciton resonances to enhance the optomechanical interaction. Typically, to maximize the photon-exciton strong coupling the QWs are positioned at anti-nodes of the cavity-confined electromagnetic field (E). In order to display strong optomechanical phenomena as considered in this work, however, the embedded quantum wells (QWs) need to be displaced away from the position of the maximum cavity optical field. It turns out that at the position of the maximum of the optical field the strain associated with the confined phonon field (s) is zero,

and thus the exciton-mediated polariton-phonon coupling vanishes. Exciton-photon strong coupling and optomechanical interactions are both optimized simultaneously if the QWs are positioned at the spacer positions where the product $s|E|^2$ is maximum. The parameters we will use in our model calculations correspond to realistic values for these optimized optomechanical cavity-polariton resonators [31–33, 35, 49].

The system we are describing displays synchronization behavior [39–43]. We will first base our discussion in previous developments in this domain, extending them later to the case of a dynamical mechanically-mediated inter-trap coupling. For that purpose we describe, as schematized in Fig. 1, two coupled polariton modes ($j = 1, 2$) and the corresponding reservoir's densities as [39]

$$\begin{aligned} i\dot{\psi}_j &= (\omega_j + U_j^P|\psi_j|^2 + U_j^R n_j)\psi_j - J\psi_{3-j} + \\ &\quad + \frac{i}{2}(Rn_j - \gamma)\psi_j, \\ \dot{n}_j &= P_j - \gamma_R n_j - R|\psi_j|^2 n_j. \end{aligned} \quad (1)$$

Here ω_j is the bare frequency of the j -mode, U_j^P and U_j^R are the polariton-polariton and reservoir-polariton interaction coupling rates, respectively, J describes a direct hopping rate term between modes (determined by the potential $V(x, t)$ in Fig. 1), γ the polariton decay rate and R the stimulated loading from the reservoir. The dynamic of the later is controlled by the pump power P_j , the excitonic decay rate γ_R and the stimulated decay rate to the condensate. Note that we operate with the angular frequencies or rates that are linked to the interaction or trap energies through the relation $\omega = E/\hbar$. We notice here that since we are considering two separate modes (on different traps) the direct overlap between them can be assumed small and consequently the equation for the local value of the reservoir density only depends on the amplitude of the corresponding polariton mode. A more involved model, including a cross term (as would be the case for a single trap) could be easily included. In that case, synchronization due to the competition of the reservoir-mediated population of the modes is also possible [40].

III. A DYNAMICAL SYSTEMS APPROACH TO THE SYNCHRONIZATION PHASE DIAGRAM

In this section we consider the case where J is time independent (that is, in the absence of a time-modulation induced by a coherent population of phonons). Even for a constant J the full model from Eq. (1) requires the analysis of a six dimensional dynamical system. However, the experiments are usually done in conditions that allow further simplifications of the model. For this purpose we assume that the reservoirs populations evolve in a faster timescale than the polaritons' dynamic, so we can perform an adiabatic approximation of the reservoirs' dynamics ($\dot{n}_j = 0$) and simplify two of the six dimensions. For a pumping rate well above condensation threshold, so that the filling rate of the polariton condensates is much faster than the exciton decay ($R|\psi_j|^2 \gg \gamma_R$), we then have $n_j \simeq \frac{P_j}{R|\psi_j|^2}$.

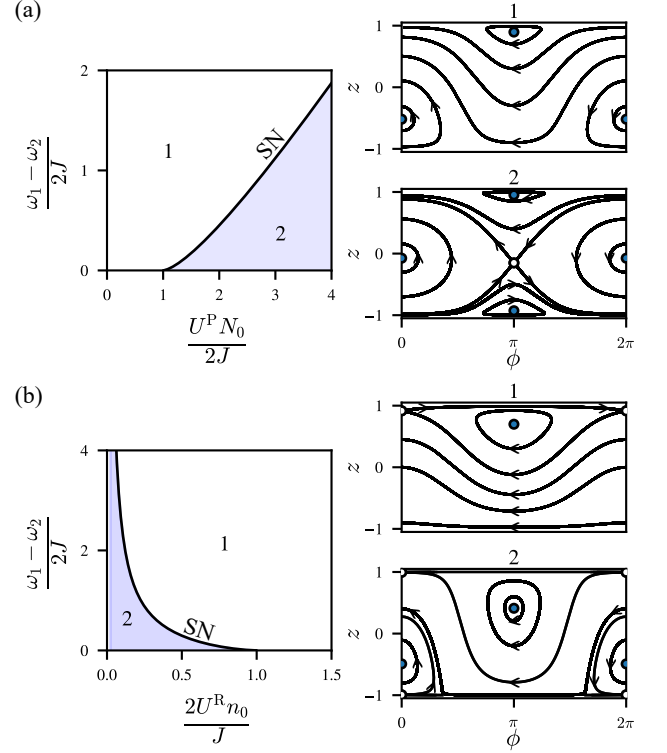


Figure 2. Bifurcation diagram for the conservative system. We show the phase portraits in the cylinder, i. e. $(\phi \bmod 2\pi, z)$. Empty dots represent saddle fixed points, blue dots non linear centers. (a) Polariton-polariton interaction only. (b) reservoir-polariton interaction only. SN stands for Saddle-Node.

Writing the mode's amplitudes as $\psi_j = \sqrt{N_j} e^{i\theta_j}$, we define two new variables $z(t) = \frac{N_1(t) - N_2(t)}{N_0}$, the fractional population imbalance, and $\phi(t) = \theta_1(t) - \theta_2(t)$, the condensates mode's phase difference, where N_0 is the total polariton population which the system approaches exponentially. For the symmetric pumping case $P_1 = P_2 = P$, the dynamical equations read:

$$\begin{aligned} \frac{dz}{d\tau} &= \sqrt{1 - z^2} \sin(\phi) - \Gamma z, \\ \frac{d\phi}{d\tau} &= -\frac{\omega_1 - \omega_2}{2J} - \alpha z + \sigma \frac{z}{1 - z^2} - \frac{z}{\sqrt{1 - z^2}} \cos(\phi), \end{aligned} \quad (2)$$

where we have performed a scaling of the time $t = T\tau$ with $T = 1/(2J)$ and defined the adimensional parameters $\Gamma \equiv \frac{\gamma}{2J}$, $\alpha \equiv \frac{U^P N_0}{2J}$ and $\sigma \equiv \frac{2U^R n_0}{J}$, with $n_0 \equiv \frac{P}{R N_0}$. A relevant quantity in the problem is the difference between the ω_j , namely, the bare detuning between the modes. The equations for $N_1 + N_2$ and $\theta_1 + \theta_2$ decouple from the equations for z and ϕ , so the effective dimension of the system is two and not four.

We are interested in finding the qualitatively different solutions of this model and the conditions under which the system synchronizes. We do this analysis using dynamical systems theory. Synchronization is reached when polaritons modes have a constant phase difference and a constant nonzero population in each state. These conditions will be satisfied for

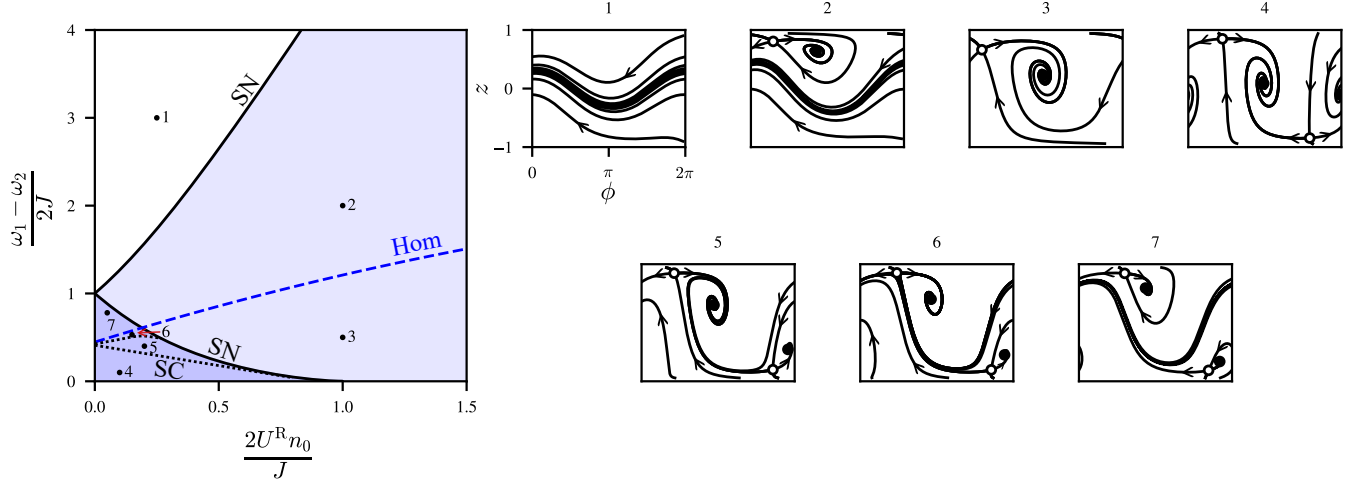


Figure 3. Bifurcation diagram of the model (Eq. (2)) in the dissipative regime. The parameters are set to $\Gamma = 0.5$, $\alpha = 0$. The bifurcation curves define 7 regions with qualitatively different dynamics. The insets show a representative phase portrait for each region. SN, Hom and SC stand for Saddle-Node, Homoclinic and Saddle-Connection bifurcations, respectively (see text for details). The vertical and horizontal axis in the right panels correspond to z and $\phi \bmod 2\pi$, respectively.

the fixed points of the problem. These points (ϕ^*, z^*) can be computed by solving the equation $f_{1,\pm}(z^*) = f_2(z^*)$ with

$$\begin{aligned} f_{1,\pm}(z) &\equiv \frac{z}{1-z^2} \left(-\sigma \pm \sqrt{1 - (1 + \Gamma^2)z^2} \right), \\ f_2(z) &= -\frac{\omega_1 - \omega_2}{2J} - \alpha z, \end{aligned} \quad (3)$$

under the condition $\Gamma|z^*| \leq \sqrt{1 - z^{*2}}$. Once z^* is computed, the phase can be obtained from the condition $\sin(\phi^*) = \frac{\Gamma z^*}{\sqrt{1 - z^{*2}}}$. One can find curves in the parameter space that separate open regions where the necessary conditions for the existence of the fixed points can be satisfied. These are called bifurcation curves. Fixed points are born through a Saddle-Node (SN) bifurcation when $f_{1,\pm}(z)$ is tangent to $f_2(z)$ at $z = z^*$, that is $f'_{1,\pm}(z^*) = f'_2(z^*)$ with

$$\begin{aligned} f'_{1,\pm}(z) &= \frac{-\sigma(1+z^2)\sqrt{1 - (1 + \Gamma^2)z^2} \pm (1 - z^2(1 + 2\Gamma^2))}{(1 - z^2)^2 \sqrt{1 - (1 + \Gamma^2)z^2}}, \\ f'_2(z) &= -\alpha. \end{aligned} \quad (4)$$

We separate our analysis in two scenarios, with and without dissipation.

Analysis of the model with no dissipation.

When $\Gamma = 0$, as for the case of quantum coherent tunneling between two atomic trapped Bose-Einstein condensates [52, 53], the system is conservative so we cannot have any attracting fixed points [54]: polariton condensates can synchronize only if there are losses.

In Fig. 2 we show the bifurcation diagram and the phase portraits considering, only polariton-polariton interaction ($\alpha \neq 0$, $\sigma = 0$, Fig. 2(a)), and only reservoir-polariton interaction ($\alpha = 0$, $\sigma \neq 0$, Fig. 2(b)). In both cases there is a region (denoted as region 1) with two fixed points. For the case with only polariton-polariton interaction (Fig. 2(a)) both

fixed points are centers while in the reservoir-polariton case (Fig. 2(b)) there is a saddle and a center. Two new fixed points are born through a SN bifurcation (in region 2). In the first case the fixed points are born in $\phi = \pi$, while in the second one they appear in $\phi = 0$.

Analysis of the model with dissipation. Figure 3 shows the bifurcation diagram for $\Gamma \neq 0$ [4, 5, 55] and taking into account only the reservoir-polariton interaction—similar dynamics is found for a dominant polariton-polariton interaction. As the system is invariant under the transformation $(z, \phi, \frac{\omega_1 - \omega_2}{2J}) \rightarrow (-z, -\phi, -\frac{\omega_1 - \omega_2}{2J})$ we restrict our analysis to $\frac{\omega_1 - \omega_2}{2J} > 0$.

In region 1, at high bare detuning, no fixed points exist and all initial conditions evolve to a stable limit cycle (the so-called Josephson oscillations). In region 2, two fixed points are born through a SN bifurcation, of course this means that one of them is a stable fixed point. Interestingly, we find that synchronization can appear for these parameters. If the system starts at the basin of attraction of the stable fixed point, the condensates synchronize, otherwise the system converges to a Josephson oscillation. This is consistent with Ref. [39]’s reported nonzero probability for the system not to reach a synchronized state. Then, we find that at the dashed curve labeled as “Hom”, the limit cycle collides with the saddle point and disappears through a Homoclinic bifurcation. For bare detuning below this curve, at region 3, the system synchronizes for all initial conditions, i.e., there exists a single stable fixed point. Indeed, these three regions dominate the map and are very similar to the main regions (or tongues) we discuss on the following sections (e.g., see Fig. 4 below).

For the sake of completeness, we also mention the existence of other regions in Fig. 3’s map which have a much smaller dominance in the parameter space. For example, in region 4, two new fixed points are born in a SN bifurcation. In regions 4, 5 and 6 the system undergoes two global bifurcations

(Saddle-Connections labeled as "SC") in which the invariant manifolds of the saddle points are reorganized. In these regions we see that, even though the bare detuning favours a higher population in the first trap, the system can converge to a state in which the second condensate is more populated. In region 7 we have two stable fixed points and a periodic orbit as attracting limit sets or *attractors*.

IV. MECHANICALLY INDUCED MODULATION IN THE COUPLING $J(t)$

The motivation to theoretically study the effects of optomechanical dynamic modulation in the context of polariton condensate synchronization is based on a series of recent experimental works describing coupled phonon and polariton coherent phenomena in non-resonantly excited arrays of polariton micrometer-size traps. This begins with the observation of polariton-driven phonon lasing [31], i.e., the establishment of self-induced coherent mechanical oscillations of $\Omega \approx 20\text{GHz}$ frequency, which were observed when a resonant condition was established tuning neighbor polariton condensates at energy differences corresponding to integer numbers of the phonon frequency Ω . These phenomena were later explained due to optomechanical parametric oscillation induced by coupling between relatively distant traps [32] quadratically proportional to the phonon displacement operator, $\hat{x} = x_{zpf}(\hat{b} + \hat{b}^\dagger)$, as given by the following optomechanical interaction Hamiltonian,

$$H_{OM} = -\hbar g_n (\hat{b} + \hat{b}^\dagger)^n (\hat{\psi}_1^\dagger \hat{\psi}_2 + \hat{\psi}_2^\dagger \hat{\psi}_1), \quad (5)$$

taking $n = 2$, where g_2 is the optomechanical second order coupling, and \hat{b} and $\hat{\psi}_i$ are the bosonic annihilation operators for the phonon and polariton modes, respectively. In principle also phonon lasing involving an inter-trap optomechanical coupling that is linear in the phonon displacement, i.e., taking $n = 1$ in Eq. (5), can exist and dominate, for traps that are closer to each other so that there is a finite direct coupling, as previously reported for coupled photonic microdiscs [56]. Such linear optomechanical inter-trap interaction, g_1 , has however not been observed to date, to the best of our knowledge, in the context of coupled polariton condensates. Very recently it was also reported a very stable locking of the relative frequencies between polariton traps in arrays [33]. This latter phenomenon resembles that of synchronization, but it contrasts with it in that the energies corresponding to neighbor polariton condensates do not become equal. Instead, they intriguingly get stabilized as the excitation power increases, with differences corresponding to integer multiples of the phonon frequency Ω . All these previous experiments signal the self-induced establishment of coherent mechanical oscillation for continuous wave and non-resonant laser excitation above the threshold for condensation in coupled polariton fluids. Notably, these resonant bulk acoustic waves in the GHz range can also be electrically generated [35, 36], opening the path to electrical high-frequency modulation of polariton condensate arrays.

To investigate these phenomena we now consider the case described by Eq. (1) but when the coupling constant J encodes the time-dependent modulation produced by a coherent mechanical wave of frequency Ω and period $T = 2\pi/\Omega$. In the case of relatively distant traps the direct coupling can be considered null between traps ground states (as e.g. described by the experiments in Ref. 33). It then becomes relevant an inter-trap coupling that is quadratic in the phonon displacement (and which requires an excited polariton state that extends between the two traps [32]), leading to a time dependent hopping $J(t) = J_2(e^{i2\Omega t} + e^{-i2\Omega t} + 2)$ with $J_2 = g_2 n_b$. This follows from assuming the presence of a coherent population of n_b phonons, i.e., $b(t) + b(t)^* = 2\sqrt{n_b} \cos(\Omega t)$, and the interaction Hamiltonian of Eq. (5) with $n = 2$. The periodicity in this case is $T/2$. On the other hand, if the two traps were closer to each other, direct inter-trap coupling could arise and Eq. (5) with $n = 1$ (the linear case) would lead to the T -periodic $J(t) = J_1(e^{i\Omega t} + e^{-i\Omega t})$ where $J_1 = g_1 \sqrt{n_b}$.

A. Rotating Wave Approximation Approach

The full implications of the time periodicity of $J(t)$, both the linear and quadratic cases, are presented in the next section. However, a first glimpse to its effects can be captured analytically by applying the rotating wave approximation to the equations of motion:

$$\begin{aligned} i\dot{\psi}_1 &= (\omega_1 + U_1^P |\psi_1|^2 + U_1^R n_1) \psi_1 - J(t) \psi_2 + \\ &\quad + \frac{i}{2} (R n_1 - \gamma) \psi_1, \\ i\dot{\psi}_2 &= (\omega_2 + U_2^P |\psi_2|^2 + U_2^R n_2) \psi_2 - (J(t))^* \psi_1 + \\ &\quad + \frac{i}{2} (R n_2 - \gamma) \psi_2, \end{aligned} \quad (6)$$

i.e., taking $J(t) \approx J_n e^{in\Omega t}$. This RWA is valid for small values of J_n and for detunings not too far from the resonance condition $\omega_2 - \omega_1 = n\Omega$ in which the non resonant terms of $J(t)$ can be neglected. Then the results for time-independent J of Eq. (1) can be readily used after writing $\psi_1 = \sqrt{\rho_1} e^{-i\omega_1 t + i\theta/2}$ and $\psi_2 = \sqrt{\rho_2} e^{-i(\omega_2 + n\Omega)t - i\theta/2}$. The synchronization conditions are equivalent to the ones given above (Eq. (A5)) but here one obtains $\omega_2 = \omega_1 + n\Omega + f(\theta)$ and the detuning becomes:

$$\bar{\varepsilon}_2 - \bar{\varepsilon}_1 = n\Omega + J_n \cos(\theta) \left(\frac{1}{\alpha} - \alpha \right). \quad (7)$$

In this way the conclusions for a time-independent J , as given in detail in Appendix A, apply directly by noting that the synchronized state described there maps to a mechanically induced *asynchronous* locking: the dressed frequencies of the two polariton modes, $\bar{\varepsilon}_1$ and $\bar{\varepsilon}_2$, appear separated by Ω or 2Ω for the linear or the quadratic case, respectively. Notice that within this RWA locked state each mode has a single frequency peak (without any sidebands) and also,

$$z(t) = \text{const}, \quad \phi(t) = n\Omega t + \phi_0, \quad (8)$$

which, as we show below, are conditions that do not hold for large interactions and/or large J_n . Interestingly, asynchronous locking behavior of this type has been reported recently in a completely different setting. Indeed, it was observed that the Great Kiskadee (*Pitangus sulphuratus*), a bird from the Americas, manages to lock the frequency difference between its two vocal cords. The mechanics of this bird's singing responds to non-linear dynamical equations very similar to those used above to describe the coupled condensates [57].

B. Full model and numerical simulations

In this section we explore the polaritons' dynamics beyond the rotating wave approximation. When solving Eq. (6) we assume identical interaction strengths in both traps, i.e., $U_1^P = U_2^P = U^P$ and $U_1^R = U_2^R = U^R$. As we see below this approximation suffices to explore the richness of the asynchronous locking phenomena. The non-resonant laser drives the exciton reservoir of the two traps providing the gain that populates the polariton modes. To quantify such gain, we define the polariton density that would be produced in the strongly condensed limit as $\bar{\rho}$, and the reservoir densities become $n_j = n_0/(P_{th}/P_j + |\psi_j|^2/\bar{\rho})$. With this notation the gain-loss factors in Eq. (6) become

$$\begin{aligned} (Rn_j - \gamma) &= \gamma(n_j/n_0 - 1) \\ &= \gamma \left(\frac{1}{\frac{P_{th}}{P_j} + \frac{|\psi_j|^2}{\bar{\rho}}} - 1 \right). \end{aligned} \quad (9)$$

As gains and losses for each mode balance the polariton populations reach, if $J(t) = 0$, $|\psi_j^{eq}|^2 = \bar{\rho}\xi_j^0/(\xi_j^0 + 1)$ where $\xi_j^0 = P_j/P_{th} - 1$ (as defined in Appendix A) or 0 below condensation. The effects of the reservoir-polariton and the polariton-polariton interactions are parameterized by the frequencies, $U^R n_0$ and $U^P \bar{\rho}$, respectively. Unless otherwise stated in what follows the gain is balanced, $P_1 = P_2 = P$, and the condensates are driven in the strongly condensed limit, $P_j/P_{th} \gg 1$, thus $(Rn_j - \gamma) \mapsto \gamma(\bar{\rho}/|\psi_j|^2 - 1)$. In this limit in absence of $J(t)$ both modes would just condensate to $|\psi_j^{eq}|^2 = \bar{\rho}$ and $z(t) = (|\psi_1|^2 - |\psi_2|^2)/(|\psi_1|^2 + |\psi_2|^2)$ would vanish in the steady state. Note that the frequency shift due to the interactions, $U^P \bar{\rho} + U^R n_0$, is identical for both modes, i.e., the bare detuning between both modes is just $\Delta\omega = \omega_2 - \omega_1$.

To investigate the effect of $J(t)$ we numerically solve the dynamics described by Eq. (6) and analyze its steady states. Given that the state-of-the-art measurement techniques allow for sub-GHz resolution spectra [58], we focus on the spectral properties of these signals. Importantly, such measurements have enough spatial resolution to identify the signals coming from each trap; this means experimental access to each $\psi_j^*[\omega]$, the Fourier transforms of each $\psi_j^*(t)$. To quantitatively and qualitatively classify the different situations we introduce the *dressed* frequency detuning between the two modes as $\Delta\tilde{\omega} = \tilde{\omega}_2 - \tilde{\omega}_1$, where each $\tilde{\omega}_j$ is defined as the frequency with maximum spectral weight in $\psi_j^*[\omega]$. As discussed above, for steady states reaching phonon-induced lock-

ing conditions, the dressed detuning departs from changing smoothly with the bare detuning $\Delta\omega$ and instead it becomes fixed to

$$\Delta\tilde{\omega} = \ell\Omega, \quad (10)$$

with ℓ being an integer or a fractional number within significant regions of the parameter space. In what follows we use labels L_ℓ to denote such $\ell\Omega$ asynchronous locked states. For example, the synchronized state for $J(t) = J$ (without phonons) presented in Sec. III corresponds to a $\ell = 0$ locking steady state, and so labeled as L_0 .

1. Integer ℓ Lockings. Linear Case.

We first investigate the main types of steady states that can be reached, focusing on integer ℓ leaving the fractional cases for later in this section. For this we sweep initial conditions $\psi_1(t_0) = \sqrt{\bar{\rho}(1+z_0)/2}$ and $\psi_2(t_0) = \sqrt{\bar{\rho}(1-z_0)/2}e^{-i\phi_0}$ on the (ϕ_0, z_0) plane (with $t_0 = -5000T$ ensuring that at $t = 0$ the steady state is already reached). We do this for the linear case of $J(t) = J_1(e^{i\Omega t} + e^{-i\Omega t})$ with the conclusions for its main lockings conditions, i.e., $\ell = \pm 1$, also qualitatively apply to the quadratic case main ones' $\ell = \pm 2$ (see Sec. IV B 2 below). We begin with values of J_1 small with respect to Ω in order to avoid effects of strong coupling and because it is consistent with previous experimental and theoretical studies. In Fig. 4(a) we present a map in the parameter space of $\Delta\omega$ and $U^R n_0$ classifying regions according to the set of solutions found by sweeping the initial conditions.

The main locking zone appears centered at bare detuning $\Delta\omega = 1$ where all initial conditions lead to the same type of locking attractor having $\ell = 1$, therefore the characteristic set for this region is just $\{L_1\}$. Indeed, such region, that broadens in detuning as the interaction strength increases, corresponds to the one predicted by the RWA transformation that maps the synchronized state of the time-independent coupling to the asynchronous locking as described in Eq. (7). However, the attractor of the full linear case differs slightly from the RWA one of Eq. (8). This can be seen in the time-dependence, trajectories and spectra of an L_1 attractor shown in Fig. 4(c): $z(t)$ is not constant but it oscillates (gray line) and each mode spectrum has weak $2\Omega n$ -separated sidebands, which are absent in the RWA solution. This panel also includes, in black dots, the Poincare map in (ϕ, z) obtained by period-sampling (with $T = 2\pi/\Omega$) the steady-state solution as sketched in the $z(t)$ dependence. For the L_1 attractor such Poincare map generates a single-point Poincare section which is a reflection of the T -periodicity of this particular attractor. The grey line shows the full trajectory of the attractor, by noticing the arrow direction one can see that ϕ advances 2π after a single period which is consistent with $\ell = +1$. Such phase advance follows from the definition of asynchronous locking and, as done below for visualization purposes, it can be discounted by moving to a rotating frame at the locking rate, i.e.,

$$\tilde{\phi}_\ell(t) \equiv \phi(t) - \ell\Omega t. \quad (11)$$

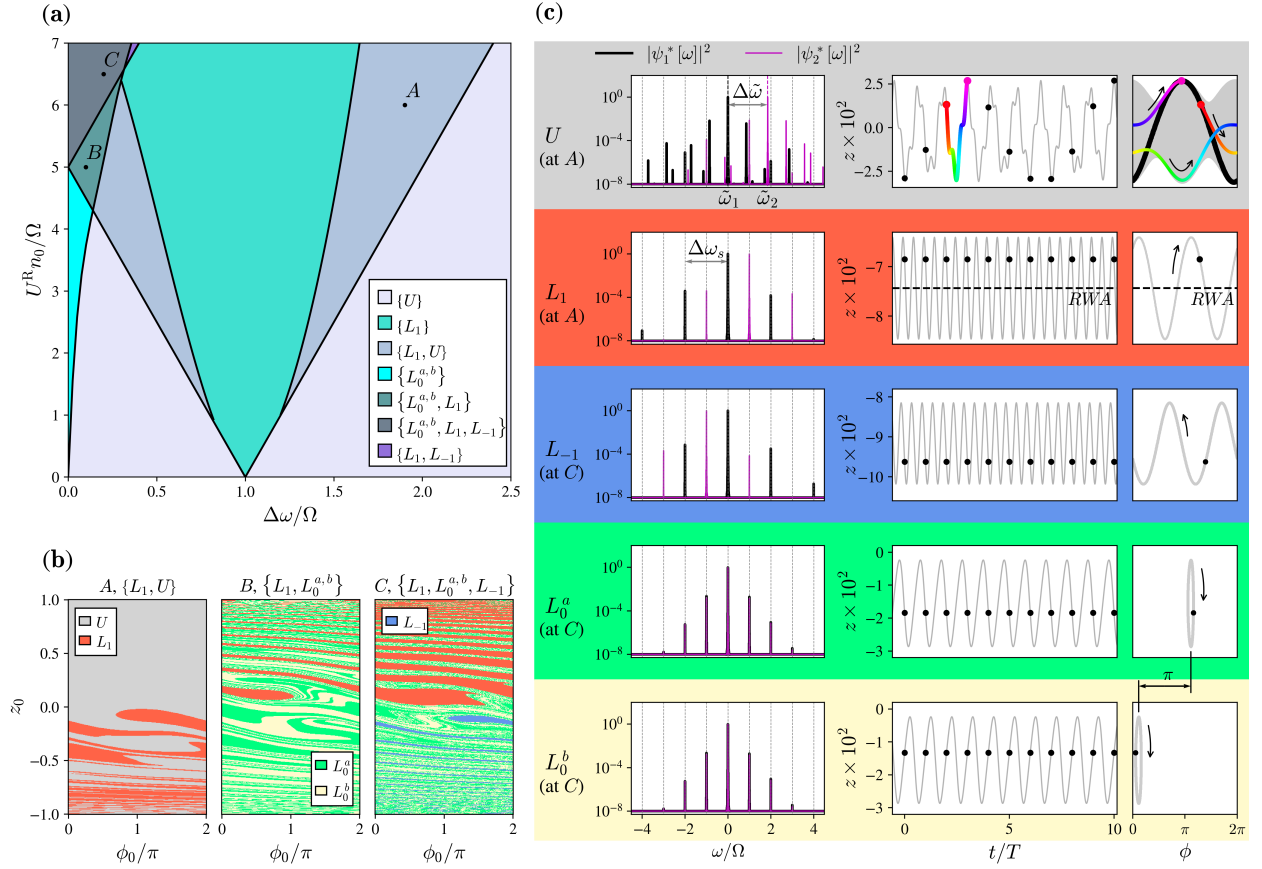


Figure 4. (a) Regions having different asynchronous locking attractors, listed in brackets (see legend), for the linear case, in the parameter space of bare detuning, $\Delta\omega$, and reservoir-polariton interaction, $U^R n_0$. Here $\gamma = 0.2\Omega$, $J_1 = \Omega/100$, $U^P \bar{\rho} = 0$ while the nonresonant-driving is assumed balanced and in the strongly condensed limit, i.e., $P_1 = P_2 \gg P_{th}$. (b) Color-coded basins of attraction obtained by sweeping initial conditions (ϕ_0, z_0) for the three exemplary points marked in panel (a) map. The complexity of the basins appears because points A, B and C correspond to 2-, 3-, and 4-attractor regions, respectively. In panel (c) each row—its color background corresponds to each one of the five types of steady-state solutions in agreement with the basins of attractions of (b)—shows: (Left) the steady-state power spectra of the two modes, $|\psi_j[\omega]|^2$ with global frequency-shifts removed for grid alignment; the dressed detuning $\Delta\tilde{\omega}$ is obtained from the frequency difference between the positions of the maximum spectral weight of each mode: $\tilde{\omega}_j$. (Center) the grey line shows the time-dependence of $z(t)$ with the sequence of black dots signaling the period sampling of the Poincare map. And (right) the associated (ϕ, z) phase space Poincare section in black and full attractor in gray with arrows showing the time-evolution direction. Note that in all panels labels L_ℓ , with $\ell = \{1, -1, 0\}$, denote solutions of having constant dressed detuning $\Delta\tilde{\omega} = \ell\Omega$ and remain *locked* in large regions of the parameter space. For *unlocked* solutions, labeled U , the dressed detuning varies smoothly (see $\Delta\tilde{\omega}$ colormaps in Fig. 5) being different to $n\Omega$. Labels L_0^a and L_0^b denote two nonequivalent attractors for the locking at $\ell = 0$ differing, as shown in (c), by a π -shifted trajectory in (ϕ, z) . Within the RWA, i.e., for $J(t) = J_1 e^{i\Omega t}$, only the $\{L_1\}$ and the two $\{L_1, U\}$ locking regions are present; in panel (c) such L_1 solution evolves along the dashed line, while for each mode only the main peak of the spectrum would remain (see Eq. (8)).

A second type of solution found in Fig. 4(a) map is the *unlocked* one, labeled U , for which the black points of the Poincare map (also shown in Fig. 4(c)) fall on a sinusoidal-like shape evidencing quasi-periodicity as the map samples additional frequency scales different from the phonon frequency Ω and its harmonics. Indeed these scales arise (exactly within the RWA or approximately for the general case) from the spectral content of the stable limit cycle of the Josephson-like oscillations described in Sec. III. The dressed detuning of such unlocked solutions varies smoothly with parameters in contrast to the fixed $\Delta\tilde{\omega}$ in locked regions (see the corresponding $\Delta\tilde{\omega}$ map Fig. 5(a)). The gray lines connecting different points of such map (i.e., the full trajectory in Fig. 4(c)) cover a large region of the (ϕ, z) phase space (we colour one

T -lasting evolution between two points of the Poincare map) in contrast to the simple trajectories found for locked attractors. This difference is also apparent from the much simpler spectra of the locked solutions for which the phonon provides a reference clock to the polaritons and not only the dressed detuning, but also the sidebands spacing of each mode, $\Delta\omega_s$, become commensurable with Ω . The unlocked solutions appear alone in the region $\{U\}$, or in coexistence with the L_1 solution in the $\{L_1, U\}$ ones (see the basins of attraction in Fig. 4(b) for point A within a $\{L_1, U\}$ zone from which Fig. 4(c) L_1 and U attractors were taken). Indeed, regions $\{U\}$, $\{L_1, U\}$, and $\{L_1\}$ can be derived from the results of time-independent J : they correspond to Fig. 3's map zones 1, 2, and 3, respectively. In particular, the synchronization tongue for Fig. 3,

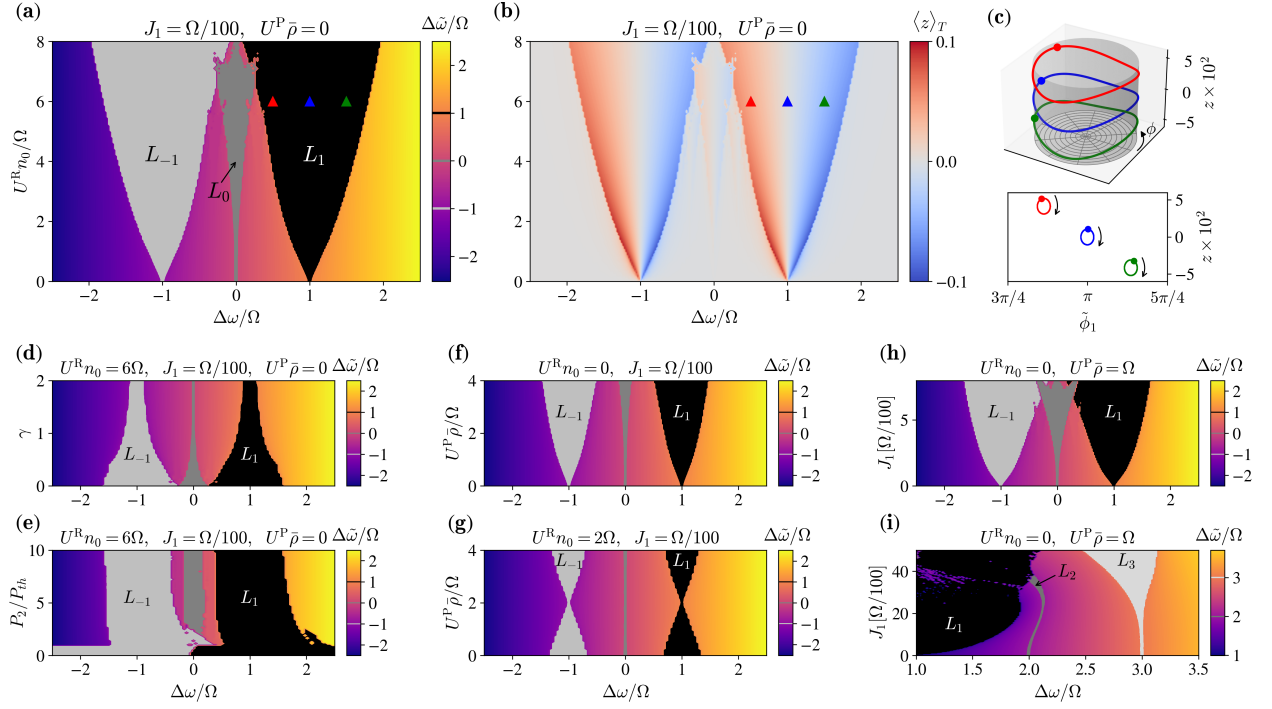


Figure 5. Behaviour of the dominant integer locking regions for $J(t)$ arising due to a coherent phonon population in presence of a *linear*-phonon inter-trap optomechanical coupling for a single representative initial condition. Unless otherwise stated the parameters are as given in Fig. 4. Colormaps of the obtained dressed detuning functionality (with main integer locked regions highlighted in gray scale) versus bare detuning $\Delta\omega$ and as a function of: (a) the reservoir-polariton interaction $U^R n_0$ —its associated map of the time-average of $z(t)$ is presented in (b)—; (d) the polariton decay rate γ for $P_1/P_{th} = P_2/P_{th} = 10$ for $U^R n_0 = 6\Omega$; (e) the degree of condensation of mode 2, P_2/P_{th} , while mode one is in the large condensation limit and $U^R n_0 = 6\Omega$; (f) [(g)] the polariton-polariton interaction $U^P \bar{\rho}$ for $U^R n_0 = 0$ [$U^R n_0 = 2\Omega$]; and (f) [(i)] the amplitude of the coupling J_1 [for larger values of J_1 and $\Delta\omega$ showing higher order locking] with $U^P \bar{\rho} = \Omega$. Panel (c) shows trajectories $z(\phi)$, for the three conditions inside the $\ell = 1$ locking tongue marked in (a) and (b). These trajectories are represented both in 3D form using cylindrical coordinates for ϕ , and in the 2D space in the rotating frame $(\hat{\phi}_\ell, z)$, i.e., discounting the phase difference $\ell\Omega t$ that arises due to the $\ell\Omega$ -frequency locking. In the latter the remaining structure reveals the sideband content of the signals (as shown in the spectrum for case L_1 in Fig. 4(c)).

centered at $\Delta\omega = 0$, corresponds to the L_1 tongue since it appears Ω -shifted in detuning by virtue of the time-dependent rotating transformation applied in Sec. IV A to solve the RWA version of the coupling: $J(t) = J_1 e^{i\Omega t}$. Similarly, the counter-rotating term of the linear coupling, $J_1 e^{-i\Omega t}$, generates identical regions but involving L_{-1} , due to locking $\ell = -1$, centered at bare detuning $-\Omega$, see for example Fig. 5(a).

Figure 4(a) also shows that the full $J(t)$ produces $\ell = 0$ locking in a region near bare detuning zero. By exploring initial conditions (not shown) we found two different $\ell = 0$ attractors, labeled by L_0^a and L_0^b , for which exemplary cases are presented in Fig. 4(c). Their phase space trajectories, separated by a π phase, are not a single fixed point as in the case of perfect synchronization of Sec. III, which is also evidenced by the presence of Ω -separated sidebands in the associated spectra. As it also applies for the fractional ℓ lockings discussed below, this locking condition is induced by the nonlinearity of the interaction (the width of the region grows with $U^R n_0$) and, in this particular case, it appears at a bare detuning region being in between the two principal locking tongues (since $\ell = 0$ is the first element in the Farey sequence for the linear case discussed in Sec. IV B 3 below). For simplicity in Fig. 4(a)

we omit a very thin intermediate region at the frontier between the $\{L_0^{a,b}\}$ region and the unlocked one, $\{U\}$, in which both type of solutions can be reached.

Additionally, the map in Fig. 4(a) shows that when the interaction grows the $\{L_0^{a,b}\}$ region encounters the continuation of one $\{L_1, U\}$ one and what survives at their intersection is a region that does not contain the unlocked solution, i.e., the $\{L_0^{a,b}, L_1\}$ region. The basins of attraction for point B lying inside such 3-attractors region is shown in Fig. 4(b). With slightly higher interactions, the $\ell = -1$ attractor reaches the positive detuning region (for $U^R n_0/\Omega \approx 5$ when concurrently the L_1 one reaches $\Delta\omega = 0$ and enters the negative detuning area) coexisting with other attractors in the zones $\{L_1, L_{-1}\}$ and $\{L_0^{a,b}, L_1, L_{-1}\}$. Figure 4(b) also contains the basins of attraction for point C in the latter region, with the L_0^a , L_0^b and L_{-1} attractors shown in Fig. 4(c) corresponding to this point.

As a particular remark, we mention that the existence of regions with different type and amount of stable attractors naturally leads to hysteresis effects when a parameter is experimentally changed slowly (with respect to γ^{-1}). For example for a path in parameter space starting at region $\{L_1\}$ that then visits the $\{L_1, U\}$ region, the system would stay at a L_1 -

like attractor until the path reaches the $\{U\}$ region where the unlocked solution becomes the only stable steady-state. In contrast, along the reverse path the unlocked solution is maintained until the path enters the $\{L_1\}$ region. Though in this work we do not discuss further hysteresis phenomena, this kind of analysis is relevant and must be considered for each particular sweeping parameter path applied in a experimental setting.

In Fig. 5 we explore the behavior of the main locking regions with relevant parameters for the linear case. As in what follows we focus on the regions that can be reached without tuning the initial condition, such as $\{L_1\}$ above, we can use a single initial condition. We chose, without affecting the qualitative conclusions, $\phi_0 = \pi$ and the z_0 corresponding to $|\psi_1^{\text{eq}}|^2$ and $|\psi_2^{\text{eq}}|^2$. Figure 5(a) presents the dressed detuning colormap for the case introduced in Fig. 4 having $U^P \bar{\rho} = 0$, $\gamma = 0.2\Omega$ and $J_1 = \Omega/100$. The main locking regions show fixed steps where $\Delta\tilde{\omega} = \ell\Omega$ with ℓ equal to 1 and -1 and the corresponding bare detuning widths grow with the interaction strength $U^R n_0$; the same is true for the thinner locking tongue with $\ell = 0$. Figure 5(b) shows the associated map for the time-average of $z(t)$, $\langle z \rangle$, which becomes nonzero for bare detuning away from the center of each tongue. This can be understood as a requirement for the dressed detuning to be locked since, for $P_1 = P_2 \gg P_{th}$,

$$\begin{aligned} \Delta\tilde{\omega} &\approx \Delta\omega + U^P \langle |\psi_2|^2 - |\psi_1|^2 \rangle + U^R n_0 \left(\frac{\bar{\rho}}{|\psi_2|^2} - \frac{\bar{\rho}}{|\psi_1|^2} \right) \\ &\approx \Delta\omega - 2U^P \bar{\rho} \langle z \rangle + 2U^R n_0 \langle z \rangle, \end{aligned} \quad (12)$$

which considers the contribution of the diagonal terms of the equations of motion and, for $J_1 \ll U^R n_0$ and/or $J_1 \ll U^P \bar{\rho}$, is a reasonable approximation of the dressed detuning. Since in this particular case only $U^R n_0$ is nonzero it then follows that $\langle z \rangle < 0$ (> 0) for bare detunings $\Delta\omega - \ell\Omega > 0$ (< 0), i.e., in the superior (inferior) half of the corresponding ℓ -locking tongue. Such trend in $\langle z \rangle$ is also observed in the trajectories for the three exemplary points within the L_1 tongue shown in Fig. 5(c), in particular the one at the middle of the tongue has $\langle z \rangle = 0$.

With the dressed detuning panels (d) and (e) of Fig. 5 we further investigate the locking regions dependence with γ (for $P_1 = P_2$) and with P_2/P_{th} , respectively, for fixed interactions and amplitude of the mechanical-induced coupling, J_1 . Since we take $P_1/P_{th} = 10$ in both cases, we use the gain expression Eq. (9) instead of the strongly condensed limit. As expected from the RWA mapping to the known results of time-independent J given in Sec. III, the widths of the locking decrease with increasing γ . Otherwise, these widths remain almost constant when one of the modes is less condensed than the other. We see that even for small J_1/Ω the interaction makes the asynchronous locking a robust feature, as it is the case of the synchronization discussed in Sec. III [39]. On the other hand, for $P_2/P_{th} < 1$ the regions with $\ell = 1$ and $\ell = -1$ occupy the whole parameter space but, in contrast to the $P_2/P_{th} > 1$ region, this frequency locking is not related to the arrangement of two self-sustained oscillators. To understand this notice that, for $P_2/P_{th} < 1$, if mode 2 were isolated its losses would surpass the gains and it would be empty, i.e., it

is not a self-sustained oscillator. The amplitude of the strongly populated mode 1, $\psi_1(t)$ —which, if we neglect mode 2, can be approximated as $\psi_1(t) = |\psi_1^{\text{eq}}| e^{-i\omega_1 t}$ where ω_1 includes the effect of the local interactions—enters to the equation of motion of the empty mode 2 multiplied by $J(t)$. Mode 2 then becomes a forced oscillator subject to a two-tones driving of frequencies, $\omega_{\pm} = \omega_1 \pm \Omega$. It follows that $\Delta\tilde{\omega}$ can only be $\ell\Omega$ with $\ell = 1$ or $\ell = -1$ depending on which tone dominates and becomes $\tilde{\omega}_2$. As the mode natural frequency is $\omega_2 = \Delta\omega + \omega_1$ comparison with ω_{\pm} leads to $\text{sign}(\ell) = \text{sign}(\Delta\omega)$.

Moving to Fig. 5(f) we see that the dependence of the dressed detuning on $U^P \bar{\rho}$ for $U^R n_0 = 0$ shares all features discussed above. The change in $U^P \bar{\rho}$ can be experimentally realized by a change in power for constant U^P —within the strong condensation limit this can be simulated by a direct variation of $\bar{\rho}$. The competition between the two interactions can be seen in Fig. 5(g) where $U^P \bar{\rho}$ is modified while $U^R n_0 \neq 0$ is kept constant. For small $U^P \bar{\rho}$ the width of the locking regions is enhanced by the dominance of $U^R n_0$ then, as $U^P \bar{\rho}$ grows, the width decreases up to a minimum in which both interactions neutralize each other, then for larger $U^P \bar{\rho}$ the enhancement due to polariton-polariton interaction dominates and the width of the locking region grows again. This competence between the two contributions follows the approximation to the dressed detuning given in Eq. (12).

A natural way to increase the width of the locking regions is increasing J_1 when either the opto-mechanical coupling or the coherent population of the phonon grows. In Fig. 5(h) and (i) we fix the interactions and explore the dependence of $\Delta\tilde{\omega}$ as a function of J_1 . This panel shows growing widths of locking regions with $\ell = \pm 1$ and $\ell = 0$, which is, of course, a positive feature for the experimental observation of the effect even when the interaction is moderate. At larger values of J_1 the locked zones overlap and, as depicted in Fig. 4, the system converges to different available attractors based on the initial conditions. For very strong coupling and/or strong interactions chaotic behavior can appear as it is discussed below. At larger bare detunings, however, strong J_1 amplitudes can enable non-chaotic higher order asynchronous locking conditions, e.g., see $\ell = 3$ tongue in Fig 5(i). The fact that even-order ℓ are virtually absent can be understood by noting that $J(t)$ weights the component of the Hamiltonian proportional to a σ_x -like Pauli matrix operator in the subspace of mode 1 and mode 2. While odd orders lead to the mode mixing operator σ_x , the even orders of σ_x are proportional to the identity operator. It follows that even orders of the $J(t)$ weighted operator do not produce nontrivial inter-mode behavior, including frequency locking, because the identity operates equally on both modes.

2. Integer ℓ Lockings. Quadratic Case.

So far we have discussed the linear case in which $J(t) = J_1(e^{i\Omega t} + e^{-i\Omega t})$. The fact that the widths of the locking regions grow with the interactions, the coupling amplitude and γ^{-1} also applies in the quadratic case of $J(t) = J_2(e^{i2\Omega t} + e^{-i2\Omega t} + 2)$. By virtue of the duplication of the frequency the

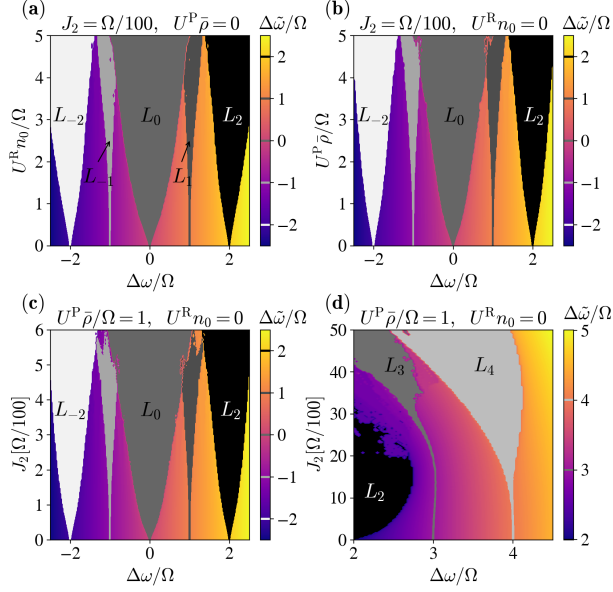


Figure 6. Behaviour of the dominant integer locking regions for $J(t)$ arising due to a coherent phonon population in presence of a *quadratic*-phonon intertrap optomechanical coupling for a single representative initial condition. Unless otherwise stated the parameters are as given in Fig. 4. Colormaps of the obtained dressed detuning functionality (with main locked regions highlighted in gray scale) versus bare detuning $\Delta\omega$ and as a function of: (a) the reservoir-polariton interaction $U^R n_0$ with $U^P \bar{\rho} = 0$; (b) the polariton-polariton interaction $U^P \bar{\rho}$ for $U^R n_0 = 0$; and (c) [(d)] the amplitude of the coupling J_2 [for larger values of J_2 and $\Delta\omega$ showing higher order locking] with $U^P \bar{\rho} = \Omega$ and $U^R n_0 = 0$. In contrast to the linear case of lockings ± 1 here the main integer tongues correspond to lockings $\ell \in \{2, 0, -2\}$ while for larger amplitudes the $\ell = 4$ locking dominates over $\ell = 3$ of the linear case.

main locking regions present $\ell = \pm 2$, centered at bare detuning $\ell\Omega$, instead of the $\ell = \pm 1$ ones of the linear case. Another important difference arises from the mechanically-induced time-independent intermode-coupling of amplitude $2J_2$ contained in $J(t)$: a $\ell = 0$ locking tongue appears as a direct manifestation of the synchronization due to time independent hopping described in Sec. III. Such region, centered at zero bare detuning, is two-times wider than the ones at $\pm 2\Omega$ because the $e^{\pm i 2\Omega t}$ factors in $J(t)$ are half than the time-independent component. This can be observed in the $\Delta\tilde{\omega}$ maps presented in Fig. 6(a) and (b) as a function of the interactions for fixed J_2/Ω and as a function of J_2/Ω in Fig. 6(c) and (d).

An additional feature of the quadratic case is that the first observed higher amplitude nonlinear effects are the appearances of $\ell = \pm 1$ tongues of smaller widths, centered at bare detuning $\ell\Omega$. As discussed in Sec. IV B 3 for fractional ℓ cases, these $\ell = \pm 1$ conditions are conceptually similar to the $\ell = 0$ tongue appearing in the linear case for detuning at the middle of two frequencies components of the driving. Furthermore, at larger detunings and larger J_2/Ω , as shown in Fig. 6(d), a $\ell = 4$ tongue appears (notice this corresponds to two times

the driving frequency 2Ω). Note this is different to the linear case in which only high-order tongues with odd multiples of the driving frequency (Ω for that case) were significant. Indeed we have checked that in the quadratic case locking regions with $\ell = 2n$ appear without distinction between odd and even n . This can be understood by noting that in this case the odd powers of the interaction Hamiltonian (which can be thought as a Pauli matrix $\sigma_x^{2n+1} = \sigma_x$, i.e., nontrivially acting in the pseudo-spin space of trap 1 and trap 2) present weights that arise from $(2J_2 + 2J_2 \cos(2\Omega t))^{2n+1}$ so they do not exclude even powers of the driving frequency 2Ω . Of course, the higher the order involved in each case, the larger the J_2/Ω required for obtaining a significant width of the corresponding $\ell = 2n$ locking region. Figure 6(d) also shows a less dominant $\ell = 3$ locking region, this belongs to the $\ell = 2n + 1$ conditions which are explicit nonlinear and high amplitude induced lockings involving multiples of the driving frequency.

3. Fractional ℓ Lockings, period-doubling and chaos.

In this section, in order to explore the lockings at fractions of the driving frequency, we increase the coupling amplitude and present detailed colormaps of the dressed detuning together with exemplary spectra and trajectories in Fig. 7. Panel (a) focuses on the linear coupling case for bare detunings between 0 and Ω with $J_1/\Omega = 0.05$ and different values of the $U^R n_0$ interaction (the dependence as a function of $U^P \bar{\rho}$ is qualitatively equivalent). Notice that a cut along $\Delta\omega$ at a fixed $U^R n_0$ visits sequentially zones of constant $\Delta\tilde{\omega} = \ell\Omega$ including fractional ℓ values, i.e., it follows a Devil staircase-like structure [59]. This is due to Arnold tongues L_ℓ with fractional values of ℓ subdividing the frequency range fixed by the main integer ℓ tongues, here $\ell = -1$ and $\ell = 1$. Besides the L_0 tongue that lies at the middle of them, which has been discussed above (as the first locking condition that is due to beyond-RWA physics) the next dominant fractions appearing in order of significance are $L_{\frac{1}{3}}, L_{\frac{1}{2}}, L_{\frac{1}{5}}$ and $L_{\frac{3}{5}}$ (tongues with denominators larger than 5 exist but they are not visible due to lack of resolution).

This type of Arnold tongues arises as a common feature induced by nonlinear effects in periodic-driven oscillators when two driving frequencies are present, for example in this case $J(t)$ contains frequency components at $-\Omega$ and Ω . Then one is to expect dressed detuning locked at fractional values subdividing such 2Ω range, i.e., in $n > 1$ parts of $2\Omega/n$. For example, the widest $n > 1$ tongue one encounters corresponds to $n = 2$ and, since this lies at $-\Omega + 2\Omega/2 = 0$, it corresponds to the $\ell = 0$ locking discussed above. Similarly, for $n = 3$, tongues at dressed detunings $-\Omega + 2k\Omega/3$ are expected, with $k = 1, 2$, where the case with $k = 2$ corresponds to the $\ell = \frac{1}{3}$ tongue found in Fig. 7(a).

Importantly, irrespective of the value of k , n fixes the side-band frequency spacing of each mode for the linear case, $\delta\omega^{(1)}$. Indeed, $\delta\omega^{(1)} = 2\Omega/n$: for example it is Ω for the $\ell = 0$ case corresponding to $n = 2$ as shown in Fig. 4(c), and it is $\delta\omega^{(1)} = 2\Omega/3$ as shown in the spectrum of the $\ell = 1/3$ case in Fig. 7(b) corresponding to $n = 3$.

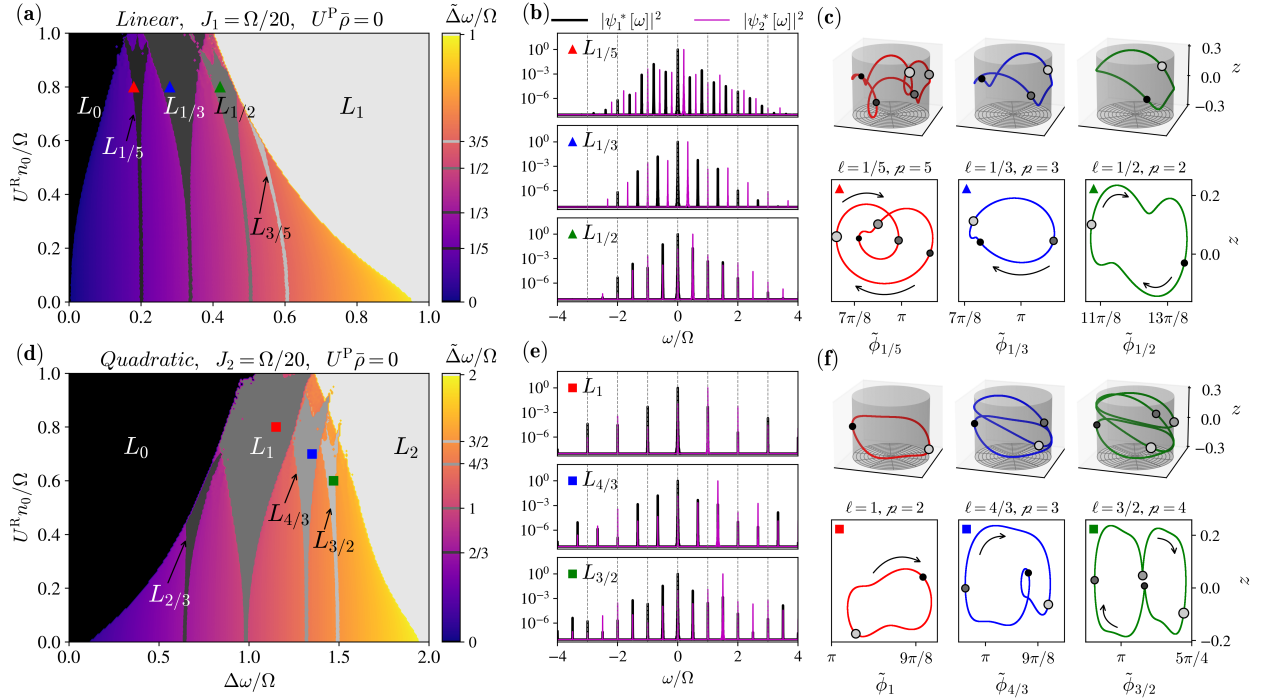


Figure 7. Exemplary fractional locking regions for both the linear and quadratic cases. (a) [(d)] Colormaps of the obtained dressed detuning functionality (with main locked regions highlighted in gray scale) versus bare detuning $\Delta\omega$ and as a function of the reservoir-polariton interaction $U^R n_0$ with $U^P \bar{\rho} = 0$ for the linear case with $J_1 = 0.05\Omega$ [quadratic case with $J_2 = 0.05\Omega$]. Panels (b) and (c) show the spectra and trajectories, respectively, for three conditions corresponding to the fractional locking tongues $\ell \in \{\frac{1}{4}, \frac{1}{3}, \frac{1}{2}\}$ of the linear case in (a). The dots at these trajectories indicate the T -periodic sampling of the Poincaré section. Panels (e) and (f) show the spectra and trajectories, respectively, for three conditions corresponding to the fractional locking tongues $\ell \in \{2 \times \frac{1}{2}, 2 \times \frac{2}{3}, 2 \times \frac{3}{4}\}$ of the quadratic case in (d). As in the quadratic case the driving frequency is 2Ω the dots at these trajectories indicate the $\frac{T}{2}$ -periodic sampling of the Poincaré section. In both (c) and (f), the 2D trajectories are presented in the rotating frame corresponding to the locking ℓ , i.e., $(\tilde{\phi}_\ell, z)$, while the full (ϕ, z) dependence is displayed in 3D-cylindrical coordinates.

In general, the linear case presents fractional tongues with $\ell = \ell_{n,k}^{(1)}$ with the definition $\ell_{n,k}^{(1)} = -1 + 2k/n$ with $k = 1, \dots, n-1$. Essentially, the sequence of lockings for all allowed k and increasing n corresponds to a Farey sequence spanned from -1 to 1 instead of from 0 to 1 [60, 61]. With this notation we can identify the remaining regions highlighted in Fig. 7(a): the $\ell = \frac{1}{2}$ one corresponds to $\ell_{4,3}^{(1)}$ whereas $\ell = \frac{1}{5}$ and $\ell = \frac{3}{5}$ correspond to $\ell_{5,3}^{(1)}$ and $\ell_{5,4}^{(1)}$, respectively. As identical locking conditions can be obtained with different subdivisions of the range, e.g., $\ell_{n,k}^{(1)} = \ell_{n \times m, k \times m}^{(1)}$ with m positive integer, this means that by exploring the nearby parameter space or the initial conditions one can encounter solutions having finer spectral subdivisions lying at the same locking region. However, the subdivision with the smallest n , and larger $\delta\omega^{(1)}$, is the one that produces the largest widening of the zone thus being prevalent, specially for smaller J_1/Ω .

The spectra shown in Fig. 7(b) for the exemplary points marked on Fig. 7(a) corroborate that the sideband spacing for each mode coincides with the corresponding $\delta\omega_n^{(1)} = 2\Omega/n$. In addition, we note that for odd n the spectral content of each mode presents weights at frequencies $\delta\omega_n^{(1)}/2 = \Omega/n$ shifted from each other, i.e., the spectral content is not overlapped, whereas the spectra of each mode lies at the same frequencies

for even n (see also the L_0 spectra in Fig. 4(c) that corresponds to $n = 2$). This can be easily understood from the fact that in the linear case $J(t)$ connects frequencies of the two modes that are separated by $\pm\Omega$ thus forcing the spectral positions of the two modes for odd- n subdivisions (since they divide 2Ω) not to appear overlapped and, therefore, inducing a $\delta\omega^{(1)}/2$ frequency shift.

For exemplary cases with $(\ell, n) \in \{(1/5, 5), (1/3, 3), (1/2, 4)\}$ Fig. 7(c) shows the corresponding time-periodic attractors either in a 3D cylindrical representation of the (ϕ, z) trajectory or in the rotating frame $(\tilde{\phi}_\ell, z)$, i.e., by discounting the locking rate $\ell\Omega t$ to $\phi(t)$ as given in Eq. (11). In both cases we include ordered dots indicating subsequent points of the Poincaré map obtained by sampling the attractor using the period of the driving, which for the linear $J(t)$ is $T = 2\pi/\Omega$, until it completes its own period. We use the number ρ to define the period of each attractor, $T_\rho = \rho T$, and find, as it can be verified by counting the dots of the Poincaré maps, that $\rho = n$ for odd n whereas $\rho = n/2$ for even n . This is also reflected in the fact that for odd n the trajectory in the rotating frame $(\tilde{\phi}_\ell, z)$ is visited twice to complete the period of the attractor T_ρ while, on the other hand, only once for even n . This is also directly linked to the above discussed $\delta\omega^{(1)}/2$ frequency shift found,

for n odd, between the two modes' spectral contents: as the trajectory follows from multiplication in the time domain of the two modes, the associated convolution in the frequency domain produces halved sideband spacing, $\delta\omega^{(1)}/2 = \Omega/n$, with respect to the even n case, thus justifying that $\rho = n$ instead of $n/2$.

By changing the $U^R n_0$ interaction energy, as done in the linear case above, in Fig. 7(d) we show the main fractional locking regions for the case of quadratic $J(t)$ with $J_2/\Omega = 0.05$ in the bare detuning region from 0 to 2Ω , i.e., in between the main locking zones of $\ell = 0$ and $\ell = 2$. As in this case $J(t)$ has spectral content at frequencies -2Ω , 0, and 2Ω , nearby frequencies also differ in 2Ω . Then expected dressed detuning lockings appear at $\Delta\tilde{\omega} = \ell\Omega$ where $\ell = \ell_{n,k}^{(2)}$ with the definition $\ell_{n,k}^{(2)} = 2k/n$, $n > 1$ and $k = 1, \dots, n-1$, associated to spectral subdivisions of $\delta\omega^{(2)} \equiv 2\Omega/n$ that produce single-mode spectral sideband spacings of the same value. In particular Fig. 7(d) highlights the zones, in order of dominance, L_1 due to $\ell_{2,1}^{(2)}$, $L_{4/3}$ due to $\ell_{3,2}^{(2)}$, $L_{2/3}$ due to $\ell_{3,1}^{(2)}$, and $L_{3/2}$ due to $\ell_{4,3}^{(2)}$. Since the spectral content of the quadratic $J(t)$ connects the two modes in frequency steps of 0 or $\pm 2\Omega$ here for both odd and even n the positions with nonzero spectral weight of the two modes coincide, as it is shown for the spectra of three cases in Fig 7(e). As the sideband spacing of the trajectory (involving mode 1 and mode 2 convolution in the frequency domain) is $2\Omega/n$ both n parities lead to periodicity of $nT/2$. Since for the quadratic coupling the duplication of the driving frequency produces a $T/2$ intrinsic periodicity we redefine $T_\rho = \rho T/2$ and, consequently, $\rho = n$ as it can be checked by counting the points of the Poincare map, sampled at $T/2$ intervals, corresponding to the trajectories shown in Fig 7(f). Note that, as expected in absence of a $\delta\omega^{(2)}/2$ frequency shift between the modes (found above for n odd in the linear case), the trajectories in the rotating frame that discounts the locking rate, $(\tilde{\phi}_\ell, z)$, are visited only once per period T_ρ regardless of the parity of n .

As mentioned above for the linear case, a given locking condition ℓ can arise with different spectral subdivisions, for the quadratic case this is just encoded in $\ell_{n,k}^{(2)} = \ell_{n \times m, k \times m}^{(2)}$ with m positive integer. A way to explore this in detail is by plotting not just the dressed detuning, as done in Fig. 8(a), but also, as shown in Fig. 8(b), $\Delta\omega_s$, defined as the sideband spacing of a single mode in the steady state. Focusing on a given fractional locking region, when the interaction grows $\Delta\omega_s$ is subject to a sequence of halving processes associated to a period doubling cascade ending with a passage to the chaotic regime: This is evidenced in Fig. 8(c), following the attractors properties along the line marked in Fig. 8(b) within the $\ell = 1$ Arnold tongue, where the Poincare map and the spectra clearly indicate the period doubling ($\rho = 2, 4, 8$, corresponding to the $\ell = 1$ lockings $\ell_{2,1}^{(2)}$, $\ell_{4,2}^{(2)}$, and $\ell_{8,4}^{(2)}$, respectively) at the $U^R n_0$ values where halvings of $\Delta\omega_s$ are observed (dashed horizontal lines). This is a prototypical example of a period doubling path to chaos where the Fourier transform complexity increases. In Fig. 8(d) we show the Poincare section for a condition in which the attractor is already chaotic and there-

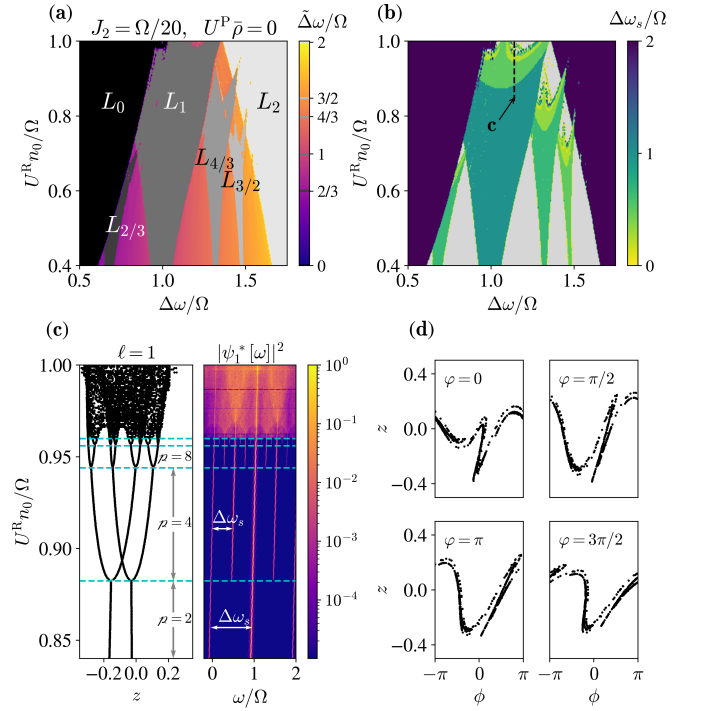


Figure 8. (a) Zoom of the dressed detuning colormap given in Fig. 7(c) for the quadratic case. (b) Corresponding colormap of $\Delta\omega_s$: the sideband spacing in the locking steady states (the unlocked region is omitted in gray). For the main locking tongues, i.e., $\ell = 0$ and $\ell = 2$, the spacing $\Delta\omega_s = 2\Omega$ is identical to driving of frequency 2Ω . Conversely, for fractional locking tongues the spacing $\Delta\omega_s$ undergoes frequency halvings as the interaction grows. Panel (c) shows the spectra for one of the modes along a vertical line inside the $\ell = 1$ fractional locking tongue, evidencing that $\Delta\omega_s$ takes values $\frac{\Omega}{2^n}$ with $n > 1$. Panel (d) values of $z(t)$ for the associated Poincare section, sampled at $\frac{T}{2}$, showing a sequence of period doubling bifurcations and the emergence of chaos. (d) Exemplary Poincare sections of a chaotic attractor, $(\tilde{\phi}_1, z)$, taken at different intra-period phases, illustrating the stretching and folding behaviour.

fore the Poincare map is no longer just ρ points of the phase space being periodically visited. The sampling points of the Poincare map are $t_n = (n + \varphi/(2\pi))T/2$, and the Poincare sections shown in Fig. 8(d) generated by maps at four different phases φ allow us to visualize a customary stretching-and-folding-like behavior in the chaotic attractor. From 8(a) one can see that despite the latter inherent chaos, the main dominant spectral components of the two modes may remain approximately locked to the ℓ of the corresponding tongue. Clearly, a coherent and predictable manipulation of the polariton modes requires avoiding entering into these chaotic conditions, though such regimes may hold interest for other applications.

V. SUMMARY

The dynamics of trapped polariton modes hosted in the discussed heterostructures can be dramatically affected by the presence of a coherent population of cavity phonons. Such

population could arise self consistently through the interaction with other degrees of freedom or from externally driven microwaves through surface or bulk acoustic wave generators. Indeed experimental evidence of locking in the polariton dynamics due to self-induced phonon populations has been reported in Ref. [33] while Ref. [34] also demonstrates polariton control using microwave-generated phonons. Depending on the situation the phonon displacement, with frequency Ω , can linearly or quadratically modulate the induced inter-mode coupling $J(t)$. To investigate the effect of this modulation on the polaritons we first revisited the situation in which the coupling is time-independent. We study the case in which both traps are non-resonantly driven by an external laser and the polariton modes condensate as independent self-sustained oscillators having its own frequencies. If the modes were uncoupled the dressed detuning just follows the bare detuning $\Delta\omega$. A time-independent coupling J between the traps allows for synchronizing the frequencies of the condensed modes in a region of bare detuning which is enlarged by either polariton-polariton or reservoir-polariton interactions as well as J/γ .

Using a rotating-wave mapping we show that the latter synchronization effect, which is analytically formulated, can explain that, for phonon-induced $J(t)$ modulation, there exist zones of bare detuning, centered at $\ell\Omega$, in which the main spectral lines of the two modes appear separated by a locked frequency of $\Delta\tilde{\omega} = \ell\Omega$, with $\ell = \pm 1$ or $\ell = 0, \pm 2$ when the coupling contains the phonon linearly or quadratically, respectively. Within these bare detuning zones—which can be enlarged by the interactions, the $J(t)$ amplitude, and the polariton lifetime γ^{-1} —the spectral signature of the steady state is the locking of the dressed detuning, $\Delta\tilde{\omega}$, at values in multiples of the phonon frequencies.

Beyond the rotating wave approximation several other effects develop. First the locking conditions persist despite the fact that the spectra of each mode present sidebands due to the presence of counter-rotating parts in $J(t)$. The initial conditions are important in regions of parameter space in which different locking attractors coexist, however, the main locking regions ($\ell = \pm 1$ for the linear case and $\ell = 0, \pm 2$ for the quadratic case) present a core with a single attractor. This fact would produce hysteresis in experiments in which parameters are swept slowly through regions with different number of stable solutions. Regarding the nature of the locked frequency states, the phase difference of the two condensates $\phi(t)$ has $\ell\Omega t$ contribution that can be discounted moving to a rotating frame, what remains is a structure related to the sideband complexity of the attractor, e.g., within the RWA this would be just a constant ϕ_0 . In the case of the relative unbalance between mode 1 and 2 occupations, $z(t)$, its time-average is zero at bare detunings $\ell\Omega$ (the center of the locking tongues) while it becomes nonzero away from such condition: with its sign depending on the dominance of polariton-polariton or reservoir-polariton interaction. This can in principle be modified by tuning the power, as the competence between $U^P\bar{\rho}$ and $U^R n_0$

adds a control knob to tune the polariton ℓ -locked states.

In the case of stronger driving at larger bare detunings additional locking conditions arise, due to higher order of the driving interaction operator, corresponding to larger integers values of $|\ell|$; in particular, for the linear case only odd ℓ cases (e.g., $\ell = 3$ in Fig. 5(i)) develop regions with significant bare detuning width. In addition a prominent non-linear effect, that cannot be accounted either with the rotating-wave argument or due to higher orders of the coupling operator, is the onset of locking values $\Delta\tilde{\omega} = \ell\Omega$ intermediate between the main locking conditions. Such fractional conditions arrange in Arnold tongues, subdividing the 2Ω ranges of the bare detuning $\Delta\omega$ in between the main locking regions and configuring typical Devil's staircase-like structures commonly found in periodic-driven nonlinear systems unveiling a Farey sequence of the corresponding ℓ values. Depending on the position of the tongue the lowest period of the attractor becomes a particular multiple of the $J(t)$ period. The bare detuning widths of those regions are also enhanced by the interactions and the amplitude of $J(t)$. Furthermore, if one of such parameters is increased, as the tongue widens the attractor sequentially undergoes period doubling processes eventually reaching chaotic behavior.

In summary, phonon-induced $J(t)$ produces a rich variety of integer and fractional locking conditions at the frequencies of the cavity phonons which in these systems range from 7–150GHz. These two-trap polariton states are ideal for being detected with state of the art spectroscopic methods involving interferometrically measuring visible light at hundreds of THz with spectral resolutions lower than 1GHz. Indeed, Ref. [33] presents experimental evidence of multi-trap phonon-induced integer ℓ locking in the polariton dynamics arising due to self-induced mechanical vibrations, while Ref. [34] reports similar effects for the polariton modes including the case of using the resource of microwave-generated phonons. We expect that further experimental efforts can provide evidence of the fractional ℓ lockings, hopefully unveiling the first fractions in the Farey sequence and a Devil's staircase-like pattern in the measured dressed detuning.

ACKNOWLEDGMENTS

We acknowledge partial financial support from the ANPCyT-FONCyT (Argentina) under grants PICT-2015-1063, PICT-2018-03255, PICT 2018-1509 and PICT 2019-0371, SECTyP UNCuyo 06/C053-T1. AAR acknowledges support by PAIDI 2020 Project No. P20-00548 with FEDER funds. GU thanks J. Tempere and M. Wouters for discussions during a research stay at UAntwerpen, partly funded by the Fund for Scientific Research-Flanders and N. Goldman for his hospitality at ULB.

Appendix A: Conditions for the existence of a synchronized state

The bifurcation diagram in Fig. 3 expresses the physical fact that it is the Josephson flow that establishes synchronization, with larger inter-trap couplings J required for increasing bare state detuning $\Delta\omega = \omega_2 - \omega_1$. It also shows that for the model of Eq. (1) synchronization can exist even without explicit non-linearities given by either U_j^P or by U_j^R (the reservoir dynamics \dot{n}_j provides in this case the non-linearity in the dissipative term for $\dot{\psi}_j$). Notwithstanding this affirmation, as displayed in Fig. 3 polariton-polariton and reservoir-polariton interactions strongly favor the emergence of the synchronized state by providing the means for the system to compensate for the intrinsic detuning $\Delta\omega$. The limit between unsynchronized and synchronized regions 1 and 2 in Fig. 3 can be analytically defined searching for the conditions of existence for a solution of the form $\psi_j = \sqrt{\rho_j} e^{-i\omega t \pm i\theta/2}$ in which the two states share the same frequency ω (here the + sign corresponds to $j = 1$ and the - sign to $j = 2$), and with $\dot{n}_j = 0$ [39]. Introducing this Ansatz in Eqs. (1) the following set of algebraic equations follows:

$$\begin{aligned} \frac{1}{\alpha} \frac{(\xi_1^0 - \xi_1)}{\xi_1 + 1} &= -2J_g \sin(\theta) \\ \frac{1}{\alpha} \frac{(\xi_2^0 - \xi_2)}{\xi_2 + 1} &= 2J_g \sin(\theta) \\ \alpha J \cos(\theta) + \omega &= \frac{U_1^R n_0 (\xi_1^0 + 1)}{\xi_1 + 1} + \xi_1 \rho_0 U_1^P \\ \frac{J \cos(\theta)}{\alpha} + \omega &= \frac{U_2^R n_0 (\xi_2^0 + 1)}{\xi_2 + 1} + \Delta\omega + \xi_2 \rho_0 U_2^P \end{aligned} \quad (\text{A1})$$

where $\alpha = \sqrt{\rho_2/\rho_1}$ and we have introduced some dimensionless parameters so that: $J_g = J/\gamma$, $\xi_j = \rho_j/\rho_0$, $\rho_0 = \gamma_R/R$, $P_j = (1 + \xi_j^0)P_{\text{th}}$, $P_{\text{th}} = \gamma\gamma_R/R$, $n_0 = \gamma/R$. We also made use of the stationary solution for the reservoir, $n_j = P_j/(\gamma_R + R\rho_j) = n_0 (\xi_j^0 + 1)/(\xi_j + 1)$.

Equations (A1) need to be solved for ξ_j , ω and θ . Notice that the first two allow for the determination of $\xi_j(\theta)$, independently of the interactions (for instance $J = 0$ implies $\xi_j = \xi_j^0$). While it is possible to find a general solution for $\xi_j(\theta)$, it involves a quartic polynomial with generic roots and, in practice, it is in general difficult to determine the one with physical meaning ($\xi_j, \alpha > 0$).

However, an analytical condition for θ can be found if one assumes that $R\rho_j \gg \gamma_R \rightarrow \xi_j \gg 1$, i.e. $P_j \gg P_{\text{th}}$, deep into the condensed regime [39]. In that case, $\xi_j + 1 \rightarrow \xi_j$ in the above equations (and for consistency the same applies to ξ_j^0). Hence, from the first two equations in Eq. (A1) one gets

$$\xi_1(\theta) = \Theta(-\theta)g(\theta) + \Theta(\theta) \frac{(\xi_1^0)^2}{(1 + 4J_g^2 \sin^2(\theta))g(\theta)}, \quad (\text{A2})$$

$$\xi_2(\theta) = \frac{(\xi_1(\theta) - \xi_1^0)\xi_2^0}{4J_g^2 \xi_1(\theta) \sin^2(\theta) + \xi_1(\theta) - \xi_1^0}, \quad (\text{A3})$$

with

$$g(\theta) = \frac{(\xi_1^0)^2}{\xi_1^0 + 2J_g \sin^2(\theta) \left(J_g (\xi_1^0 + \xi_2^0) + \sqrt{\xi_1^0 \xi_2^0 \csc^2(\theta) + J_g^2 (\xi_1^0 + \xi_2^0)^2} \right)}, \quad (\text{A4})$$

and $\Theta(x)$ the step function. The final equation that determines θ and the synchronization condition is then

$$\begin{aligned} \Delta\omega &= f(\theta) \\ &= J \cos(\theta) \left(\frac{1}{\alpha(\theta)} - \alpha(\theta) \right) + \frac{U_1^R n_0 \xi_1^0}{\xi_1(\theta)} + U_1^P \rho_0 \xi_1(\theta) - \frac{U_2^R n_0 \xi_2^0}{\xi_2(\theta)} - U_2^P \rho_0 \xi_2(\theta). \end{aligned} \quad (\text{A5})$$

Once θ is determined, the locking frequency is given by

$$\omega = \frac{\bar{\varepsilon}_1 + \bar{\varepsilon}_2}{2} - \frac{J \cos(\theta)}{2} \left(\alpha + \frac{1}{\alpha} \right), \quad (6)$$

and since

$$\bar{\varepsilon}_2 - \bar{\varepsilon}_1 = J \cos(\theta) \left(\frac{1}{\alpha} - \alpha \right), \quad (7)$$

we get

$$\omega = \bar{\varepsilon}_1 - \alpha J \cos(\theta). \quad (8)$$

Here $\bar{\varepsilon}_j = \omega_j + U_j^P \rho_0 \xi_j + U_j^R n_0 \frac{\xi_j}{\xi_j}$ are the trap frequencies

dressed by the interactions. Notice that we allowed here for different pump powers on each trap, $\xi_1^0 \neq \xi_2^0$. The resulting synchronization condition is identical to the one presented above in Fig. 3, except that the bifurcation diagram is not longer symmetric around $\Delta\omega = 0$ when $\xi_1^0 \neq \xi_2^0$.

-
- [1] G. Kurizkia, P. Bertet, Y. Kubob, K. Molmer, D. Petrosyand, P. Rabl, and J. Schmiedmayer, Quantum technologies with hybrid systems, *Proc. Nat. Acadm. Science* **112**, 3866 (2015).
- [2] J. Kasprzak, M. Richard, S. Kundermann, A. Baas, P. Jeambrun, J. M. J. Keeling, F. M. Marchetti, M. H. Szymańska, R. André, J. L. Staehli, V. Savona, P. B. Littlewood, B. Deveaud, and L. S. Dang, Bose-Einstein Condensation of Exciton Polaritons, *Nature (London)* **443**, 409 (2006).
- [3] A. Amo, D. B. D. Sanvitto, F. Laussy, E. del Valle, M. Martin, A. Lemaître, J. Bloch, D. Krizhanovskii, M. Skolnick, C. Tejedor, and L. Viña, Collective Fluid Dynamics of a Polariton Condensate in a Semiconductor Microcavity, *Nature (London)* **457**, 291 (2009).
- [4] K. G. Lagoudakis, B. Pietka, M. Wouters, R. André, and B. Deveaud-Plödran, Coherent oscillations in an exciton-polariton Josephson junction, *Phys. Rev. Lett.* **105** 120403 (2010).
- [5] M. Abbarchi, A. Amo, V. G. Sala, D. D. Solnyshkov, H. Flayac, L. Ferrier, I. Sagnes, E. Galopin, A. Lemaître, G. Malpuech, and J. Bloch, Macroscopic quantum self-trapping and Josephson oscillations of exciton polaritons, *Nature Physics* **9** 275 (2013).
- [6] I. Carusotto, and C. Ciuti, Quantum fluids of light, *Reviews of Modern Physics* **85**, 299 (2013).
- [7] M. J. Hartmann, F. G. Brandao, and M. B. Plenio, Strongly interacting polaritons in coupled arrays of cavities, *Nature Physics* **2**, 849 (2006).
- [8] K. Winkler, J. Fischer, A. Schade, M. Amthor, Robert Dall, Jonas Gessler, M. Emmerling, E. A. Ostrovskaya, M. Kamp, C. Schneider, and S. Höfling, A polariton condensate in a photonic crystal potential landscape, *New J. Phys.* **17**, 023001 (2015).
- [9] A. S. Kuznetsov, P. L. J. Helgers, K. Biermann, and P. V. Santos, Quantum Confinement of Exciton-Polaritons in Structured (Al,Ga)As Microcavity, *Phys. Rev. B* **97**, 195309 (2018).
- [10] S. Alyatkin, H. Sigurdsson, A. Askitopoulos, J. D. Töpfer, and P. G. Lagoudakis, Interaction induced point scatterer lattices and flat band condensation of exciton-polaritons, *arXiv:2007.02807* (2020).
- [11] K. P. Kalinin, and N. G. Berloff, Toward Arbitrary Control of Lattice Interactions in Nonequilibrium Condensates, *Advanced Quantum Technologies* **3** 1900065 (2020).
- [12] N. Y. Kim and Y. Yamamoto, Exciton-Polariton Quantum Simulators, D. Angelakis (eds), *Quantum Simulations with Photons and Polaritons*, Quantum Science and Technology, Springer (2017).
- [13] K. P. Kalinin, A. Amo, J. Bloch, and N. G. Berloff, Polaritonic XY-ising machine, *Nanophotonics* **9**, 4127-4138 (2020).
- [14] T. Boulier, M. J. Jacquet, A. Maître, G. Lerario, F. Claude, S. Pigeon, Q. Glorieux, A. Amo, J. Bloch, A. Bramati, and E. Giacobino, Microcavity polaritons for quantum simulation, *Advanced Quantum Technologies* **3**, 2000052 (2020).
- [15] S. Ghosh, and T. C. Liew, Quantum computing with exciton-polariton condensates, *Quantum Information* **6**, 1 (2020).
- [16] D. D. Solnyshkov, G. Malpuech, P. St-Jean, S. Ravets, J. Bloch, and A. Amo, Microcavity polaritons for topological photonics, *Optical Materials Express* **11**, 1119 (2021).
- [17] M. Maldovan, and E. L. Thomas, Simultaneous localization of photons and phonons in two-dimensional periodic structures, *Appl. Phys. Lett.* **88**, 251907 (2006).
- [18] M. Eichenfield, J. Chan, R. M. Camacho, K. J. Vahala, and O. Painter, Optomechanical crystals, *Nature* **462** 78 (2009).
- [19] M. Aspelmeyer, T. J. Kippenberg, and F. Marquardt, *Rev. Mod. Phys.* **86**, 1391 (2014).
- [20] H. Ren, M. H. Matheny, G. S. MacCabe, J. Luo, H. Pfeifer, M. Mirhosseini, and O. Painter, Two-dimensional optomechanical crystal cavity with high quantum cooperativity, *Nat. Commun.* **11**, 3373 (2020).
- [21] A. D. O'Connell, M. Hofheinz, M. Ansmann, Radoslaw C. Bialczak, M. Lenander, Erik Lucero, M. Neeley, D. Sank, H. Wang, M. Weides, J. Wenner, John M. Martinis, and A. N. Cleland, Quantum ground state and single-phonon control of a mechanical resonator, *Nature* **464**, 697 (2010).
- [22] J. D. Teufel, T. Donner, Dale Li, J. H. Harlow, M. S. Allman, K. Cicak, A. J. Sirois, J. D. Whittaker, K. W. Lehnert, and R. W. Simmonds, Sideband cooling of micromechanical motion to the quantum ground state, *Nature* **475**, 359 (2011).
- [23] J. Chan, T. P. Mayer Alegre, Amir H. Safavi-Naeini, Jeff T. Hill, Alex Krause, Simon Groblacher, Markus Aspelmeyer, and Oskar Painter, Laser cooling of a nanomechanical oscillator into its quantum ground state, *Nature* **478**, 89 (2011).
- [24] E. Verhagen, S. Deleglise, S. Weis, A. Schliesser, and T. J. Kippenberg, Quantum-coherent coupling of a mechanical oscillator to an optical cavity mode, *Nature* **482**, 63 (2012).
- [25] T. J. Kippenberg, H. Rokhsari, T. Carmon, A. Scherer, K. J. Vahala, Analysis of Radiation-Pressure Induced Mechanical Oscillation of an Optical Microcavity, *Physical Review Letters* **95**, 033901 (2005).
- [26] I. S. Grudinin, H. Lee, O. Painter, and K. J. Vahala, Phonon Laser Action in a Tunable Two-Level System, *Physical Review Letters* **104**, 083901 (2010).
- [27] A. Fainstein, N. D. Lanzillotti-Kimura, B. Jusserand, B. Perrin, Strong optical-mechanical coupling in a vertical GaAs/AlAs microcavity for subterahertz phonons and near-infrared light, *Physical Review Letters* **110**, 037403 (2013).
- [28] N. D. Lanzillotti-Kimura, A. Fainstein, B. Jusserand, Towards GHz-THz cavity optomechanics in DBR-based semiconductor resonators, *Ultrasonics* **56**, 80 (2015).
- [29] B. Jusserand, A. N. Poddubny, A. V. Poshakinskiy, A. Fainstein, and A. Lemaître, Polariton Resonances for Ultrastrong Coupling Cavity Optomechanics in GaAs-AlAs Multiple Quantum Wells, *Phys. Rev. Lett.* **115**, 267402 (2015).
- [30] M. Kobecki, A. V. Scherbakov, S. M. Kukhtaruk, D. D. Yaremkevich, T. Henksmeier, A. Trapp, D. Reuter, V. E. Gusev, A. V. Akimov, and M. Bayer, Giant Photoelasticity of Polaritons for Detection of Coherent Phonons in a Superlattice with Quantum Sensitivity, *Phys. Rev. Lett.* **128**, 157401 (2022).
- [31] D. L. Chafatinos, A. S. Kuznetsov, S. Anguiano, A. E. Bruchhausen, A. A. Reynoso, K. Biermann, P. V. Santos, and A. Fainstein, Polariton-driven phonon laser, *Nature Communica-*

- tions **11**, 4552 (2020).
- [32] A. A. Reynoso, G. Usaj, D. L. Chafatinos, F. Mangussi, A. E. Bruchhausen, A. S. Kuznetsov, K. Biermann, P. V. Santos, and A. Fainstein, Optomechanical parametric oscillation of a quantum light-fluid in a lattice, *Phys. Rev. B* **105**, 195310 (2022).
 - [33] D. L. Chafatinos, A. S. Kuznetsov, P. Sesin, I. Papuccio, A. A. Reynoso, A. E. Bruchhausen, G. Usaj, K. Biermann, P. V. Santos, A. Fainstein, Asynchronous Locking in Metamaterials of Fluids of Light and Sound, *Nature Communications* **14**, 3485 (2023).
 - [34] A. S. Kuznetsov, K. Biermann, A. A. Reynoso, A. Fainstein, and P. V. Santos, Microcavity phonoritons - a coherent optical-to-microwave interface, *Nature Communications* **14**, 5470 (2023).
 - [35] A. S. Kuznetsov, D. H. O. Machado, K. Biermann, and P. V. Santos, Electrically Driven Microcavity Exciton-Polariton Optomechanics at 20 GHz, *Physical Review X* **11**, 021020 (2021).
 - [36] A. Crespo-Poveda, A. S. Kuznetsov, A. Hernández-Máñez, A. Tahraoui, K. Biermann, and P. V. Santos, GHz guided optomechanics in planar semiconductor microcavities, *Optica* **9**, 160 (2022).
 - [37] K. Fang, Z. Yu and S. Fan, Photonic Aharonov-Bohm Effect Based on Dynamic Modulation, *Phys. Rev. Lett.* **108**, 153901 (2012).
 - [38] J. del Pino, J. J. Slim, and E. Verhagen, Non-Hermitian chiral phonics through optomechanically induced squeezing, *Nature* **606**, 82 (2022).
 - [39] M. Wouters, Synchronized and desynchronized phases of coupled nonequilibrium exciton-polariton condensates, *Physical Review B* **77**, 121302(R) (2008).
 - [40] P. R. Eastham, Mode locking and mode competition in a nonequilibrium solid-state condensate, *Physical Review B* **78**, 035319 (2008).
 - [41] John P. Moroney and Paul R. Eastham, Synchronization in disordered oscillator lattices: Nonequilibrium phase transition for driven-dissipative bosons, *Phys. Rev. Research* **3**, 043092 (2021).
 - [42] A. Baas, K. G. Lagoudakis, M. Richard, R. André, Le Si Dang, and B. Deveaud-Plédran, Synchronized and Desynchronized Phases of Exciton-Polariton Condensates in the Presence of Disorder, *Phys. Rev. Lett.* **100**, 170401 (2008).
 - [43] H. Ohadi, Y. D. V. I. Redondo, A. J. Ramsay, Z. Hatzopoulos, T. C. H. Liew, P. R. Eastham, P. G. Savvidis, and J. J. Baumberg, Synchronization crossover of polariton condensates in weakly disordered lattices, *Phys. Rev. B*, **97**, 195109 (2018).
 - [44] M. Galbiati, L. Ferrier, D. D. Solnyshkov, D. Tanese, E. Wertz, A. Amo, M. Abbarchi, P. Senellart, I. Sagnes, A. Lemaître, E. Galopin, G. Malpuech, and J. Bloch, Polariton Condensation in Photonic Molecules, *Phys. Rev. Lett.* **108**, 126403 (2012).
 - [45] M. Trigo, A. Bruchhausen, A. Fainstein, B. Jusserand, and V. Thierry-Mieg, Confinement of Acoustical Vibrations in a Semiconductor Planar Phonon Cavity, *Phys. Rev. Lett.* **89**, 227402 (2002).
 - [46] N. D. Lanzillotti-Kimura, A. Fainstein, C. A. Balseiro, and B. Jusserand, Phonon engineering with acoustic nanocavities: Theoretical considerations on phonon molecules, band structures, and acoustic Bloch oscillations, *Phys. Rev. B* **75**, 024301 (2007).
 - [47] S. Anguiano, A. E. Bruchhausen, B. Jusserand, I. Favero, F. R. Lamberti, L. Lanco, I. Sagnes, A. Lemaître, N. D. Lanzillotti-Kimura, P. Senellart, and A. Fainstein, Micropillar Resonators for Optomechanics in the Extremely High 19-95 GHz Frequency Range, *Phys. Rev. Lett.* **118**, 263901 (2017).
 - [48] F. R. Lamberti, Q. Yao, L. Lanco, D. T. Nguyen, M. Esmann, A. Fainstein, P. Sesin, S. Anguiano, V. Villafañe, A. Bruchhausen, P. Senellart, I. Favero, and N. D. Lanzillotti-Kimura, Optomechanical properties of GaAs/AlAs micropillar resonators operating in the 18 GHz range, *Opt. Express* **25**, 24437 (2017).
 - [49] N. Carlon Zambon, Z. Denis, R. De Oliveira, S. Ravets, C. Ciuti, I. Favero, and J. Bloch, Enhanced Cavity Optomechanics with Quantum-Well Exciton Polaritons, *Phys. Rev. Lett.* **129**, 093603 (2022).
 - [50] P. Sesin, A. S. Kuznetsov, G. Rozas, S. Anguiano, A. E. Bruchhausen, A. Lemaître, K. Biermann, P. V. Santos, A. Fainstein, Giant optomechanical coupling and dephasing protection with cavity exciton-polaritons, arXiv:2212.08269 [cond-mat.mes-hall]. Accepted in *Phys. Rev. Research*.
 - [51] C. Baker, W. Hease, D.T. Nguyen, A. Andronico, S. Ducci, G. Leo, and I. Favero, Photoelastic coupling in gallium arsenide optomechanical disk resonators, *Opt. Express* **22**, 14072 (2014).
 - [52] A. Smerzi, S. Fantoni, S. Giovanazzi, and S. R. Shenoy, Quantum Coherent Atomic Tunneling between Two Trapped Bose-Einstein Condensates, *Phys. Rev. Lett.* **79**, 4950 (1997).
 - [53] S. Raghavan, A. Smerzi, S. Fantoni, and S. R. Shenoy, Coherent oscillations between two weakly coupled Bose-Einstein condensates: Josephson effects, π oscillations, and macroscopic quantum self-trapping, *Phys. Rev. A* **59**, 620 (1999).
 - [54] S. H. Strogatz, *Nonlinear Dynamics and Chaos* (Addison-Wesley, New York, 1994).
 - [55] I. Marino, S. Raghavan, S. Fantoni, S. R. Shenoy, and A. Smerzi, Bose-condensate tunneling dynamics: Momentum-shortened pendulum with damping, *Phys. Rev. A* **60**, 487 (1999).
 - [56] I. S. Grudinin, H. Lee, O. Painter, and K. J. Vahala, Phonon Laser Action in a Tunable Two-Level System, *Phys. Rev. Lett.* **104**, 083901 (2010).
 - [57] J. F. Döppler, A. Amador, F. Goller, and G. B. Mindlin, Dynamics behind rough sounds in the song of the *Pitangus sulphuratus*, *Phys. Rev. E* **102**, 062415 (2020).
 - [58] G. Rozas, A. E. Bruchhausen, A. Fainstein, B. Jusserand, and A. Lemaître, Polariton Path to Fully Resonant Dispersive Coupling in Optomechanical Resonators, *Phys. Rev. B* **90**, 201302(R) (2014).
 - [59] P. Bak, The Devil's Staircase, *Phys. Today* **39**, 38 (1986).
 - [60] H.G. Shuster and W. Just, *Deterministic Chaos*, VCH Verlag, Weinheim, (1988).
 - [61] X. Wu, Y. Zhang, J. Peng, S. Boscolo, C. Finot and H. Zeng, Farey tree and devil's staircase of frequency-locked breathers in ultrafast lasers, *Nature Communications* **13**, 5784 (2022).